nature geoscience

Article

https://doi.org/10.1038/s41561-023-01285-1

Increasing contribution of nighttime nitrogen chemistry to wintertime haze formation in Beijing observed during COVID-19 lockdowns

Received: 12 October 2022

Accepted: 5 September 2023

Published online: 12 October 2023

Check for updates

Chao Yan[1,2,3,16], Yee Jun Tham[4,16] ✉, Wei Nie[2], Men Xia[3,5], Haichao Wang[6], Yishuo Guo[1], Wei Ma[1], Junlei Zhan[1], Chenjie Hua[1], Yuanyuan Li[2], Chenjuan Deng[7], Yiran Li[7], Feixue Zheng[1], Xin Chen[1], Qinyi Li[8], Gen Zhang[9], Anoop S. Mahajan[10], Carlos A. Cuevas[8], Dan Dan Huang[11], Zhe Wang[12], Yele Sun[13], Alfonso Saiz-Lopez[8], Federico Bianchi[3], Veli-Matti Kerminen[3], Douglas R. Worsnop[14], Neil M. Donahue[15], Jingkun Jiang[7], Yongchun Liu[1], Aijun Ding[2] ✉ & Markku Kulmala[1,2,3] ✉

Nitrate comprises the largest fraction of fine particulate matter in China during severe haze. Consequently, strict control of nitrogen oxides (NO_x) emissions has been regarded as an effective measure to combat air pollution. However, this notion is challenged by the persistent severe haze pollution observed during the COVID-19 lockdown when NO_x levels substantially declined. Here we present direct field evidence that diminished nitrogen monoxide (NO) during the lockdown activated nocturnal nitrogen chemistry, driving severe haze formation. First, dinitrogen pentoxide (N_2O_5) heterogeneous reactions dominate particulate nitrate (pNO_3^-) formation during severe pollution, explaining the higher-than-normal pNO_3^- fraction in fine particulate matter despite the substantial NO_x reduction. Second, N_2O_5 heterogeneous reactions provide a large source of chlorine radicals on the following day, contributing drastically to the oxidation of volatile organic compounds, and thus the formation of oxygenated organic molecules and secondary organic aerosol. Our findings highlight the increasing importance of such nocturnal nitrogen chemistry in haze formation caused by NO_x reduction, motivating refinements to future air pollution control strategies.

Air pollution is a major environmental problem in China due to its adverse effects on human health[1–3]. Since the implementation of 'Clean Air Action' in 2013, air quality in China has appreciably improved. However, severe air pollution events still occur, and the yearly average concentration of fine particulate matter less than 2.5 μm in diameter ($PM_{2.5}$) remains markedly higher than the threshold (5 μg m^{-3}) recommended by World Health Organization[4]. After a steady reduction of particulate sulfate (pSO_4^{2-}) from the strict control of SO_2 emissions,

A full list of affiliations appears at the end of the paper. ✉e-mail: thamyj@mail.sysu.edu.cn; dingaj@nju.edu.cn; markku.kulmala@helsinki.fi

https://doi.org/10.1038/s41561-023-01285-1

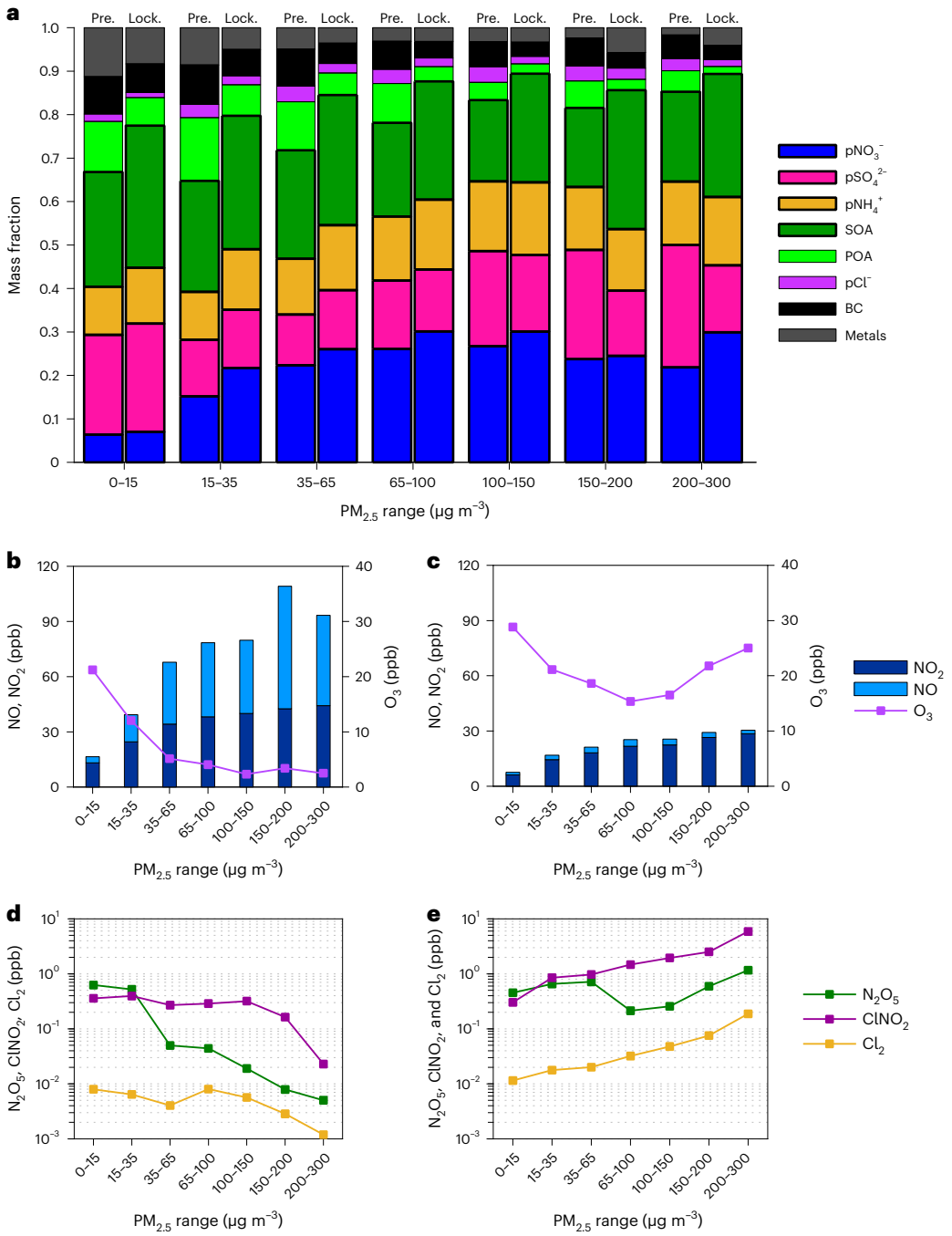

Fig. 1 | Relative contributions of $PM_{2.5}$ components and concentrations of main nitrous species in different $PM_{2.5}$ levels in the pre-lockdown and lockdown periods. a, Relative contributions of $PM_{2.5}$ components in different pollution levels. In each $PM_{2.5}$ concentration range, the left and right bars denote data in the pre-lockdown (Pre.) and lockdown (Lock.) periods, respectively. Species in bold black frames indicate secondary pollutants. POA, primary organic aerosol; BC, black carbon. **b**–**e**, Concentrations of main nitrous species in different $PM_{2.5}$ levels in the pre-lockdown (**b**,**d**) and lockdown periods (**c**,**e**).

particulate nitrate (pNO_3^-) has become the largest component of $PM_{2.5}$ during severe haze pollution in recent years[4]. Hence, stringent restriction of nitrogen oxide ($NO_x = NO + NO_2$) emissions is regarded as an effective measure to improve air quality.

To control the COVID-19 pandemic, a lockdown was imposed to create social distance, during which a dramatic reduction in NO_x concentration was observed worldwide[5–8]. This provided a unique 'real atmospheric experiment' to assess the effect of NO_x reductions on air quality. Against expectations, severe haze events still occurred during the lockdowns in China[9–11]. Even more paradoxically, during the lockdown period (23 January 2020 to 15 March 2020) when NO_x decreased by up to 60% (refs. 11–13), our measurements show that the contribution of pNO_3^- and secondary organic aerosol (SOA) increased markedly (Fig. 1a). Various modelling studies have attributed the haze during the lockdown period to an elevated atmospheric oxidative capacity and unfavourable meteorological conditions, such as high relative humidity (RH) and air stagnation[11,14,15]. However, a detailed mechanistic understanding of haze formation based on comprehensive field observations remains lacking; in particular, the paradox between NO_x reductions and haze augmentation has not been resolved.

https://doi.org/10.1038/s41561-023-01285-1

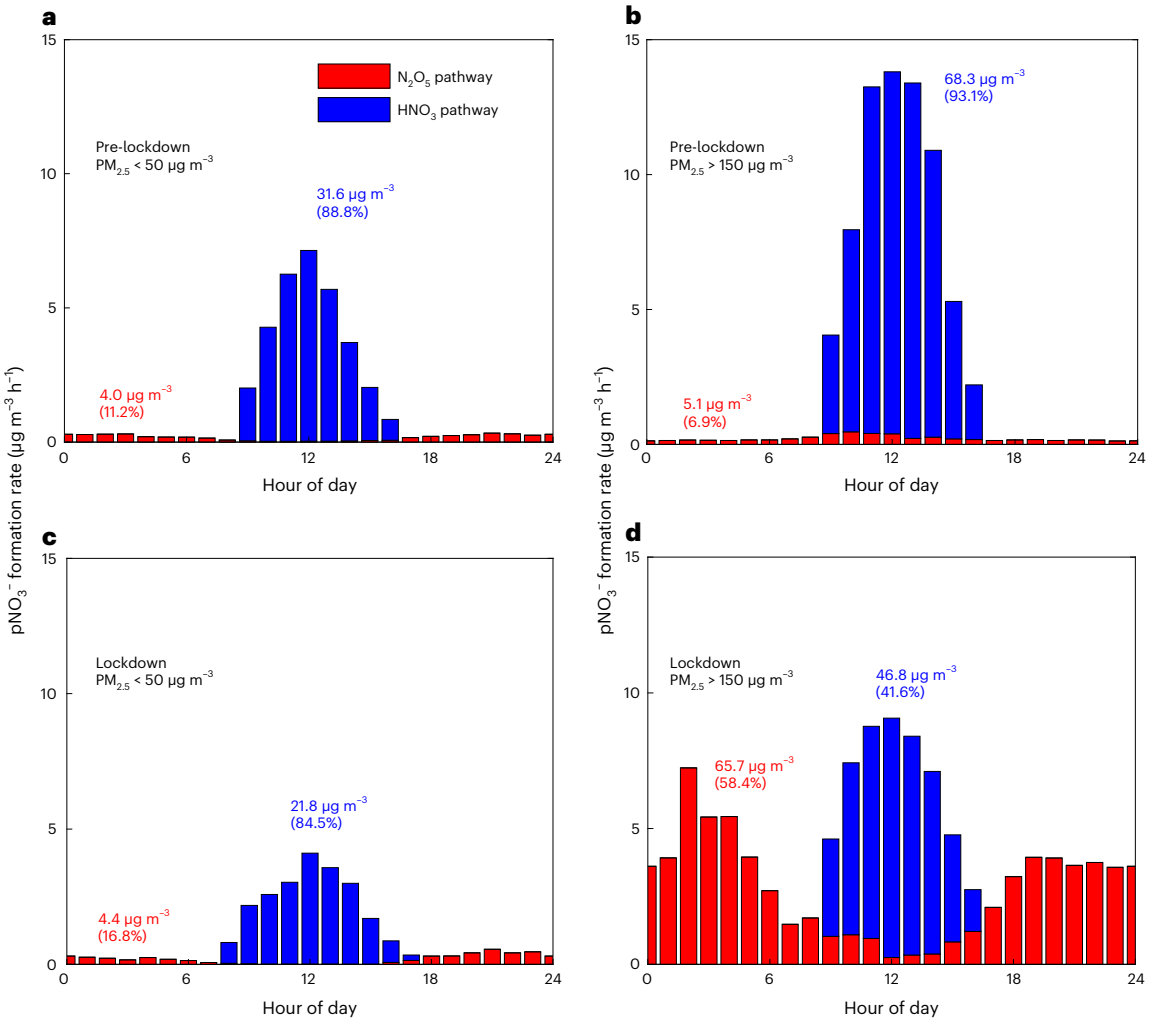

Fig. 2 | Comparison between the contributions of the HNO_3 pathway and N_2O_5 pathway to pNO_3^- formation. a–d, The results under clean conditions during the pre-lockdown (**a**), polluted conditions during the pre-lockdown (**b**), clean conditions during the lockdown (**c**) and polluted conditions during the lockdown (**d**). In all panels, the contribution of HNO_3 is calculated as the formation reaction of HNO_3 via the reaction between NO_2 and OH radicals, as almost all HNO_3 is partitioned in the particle phase. The much larger concentration of nitrate than gaseous HNO_3 supports this assumption. The N_2O_5 contribution is calculated based on the heterogeneous reaction of N_2O_5 adopting the derived uptake coefficient and $ClNO_2$ yield. The numbers in all the panels denote the total pNO_3^- formation of each pathway in 24 hours.

Enhanced nocturnal nitrogen chemistry during the lockdown

Extended Data Fig. 1 shows a time series of NO_x, ozone (O_3), $PM_{2.5}$ chemical composition, dinitrogen pentoxide (N_2O_5) and nitryl chloride ($ClNO_2$) observed during the pre-lockdown (before 23 January 2020) and lockdown period in urban Beijing. As the characteristics of these species vary markedly with pollution levels, in Fig. 1 we compare their mean concentrations in the pre-lockdown and lockdown periods at seven different $PM_{2.5}$ levels. Generally, the changes in NO_x and O_3 concentrations are consistent with those reported in previous studies (for example, ref. 12)—a substantial decrease in NO_x is associated with elevated O_3 during the lockdown period (Fig. 1b,c). In addition to the widely reported reduction of NO_x during lockdowns, a unique aspect of our observations is the drastic decline in NO. During the pre-lockdown period, NO concentrations were high (up to 200 parts per billion (ppb)), comprising a large fraction of NO_x that increased with $PM_{2.5}$ loading (Fig. 1b). In contrast, NO concentrations in the lockdown period were low regardless of the $PM_{2.5}$ loading (Fig. 1c). This is mostly because of the diminished NO emissions during the lockdown period, very probably due to greatly reduced activity by on-road vehicles. Furthermore, the diurnal patterns of NO and O_3, especially on polluted days, were completely altered during the lockdown (Extended Data Fig. 2), and nighttime NO levels were substantially reduced, coinciding with higher nighttime O_3 levels (NO titration of O_3 was no longer complete).

It is well recognized that NO_x undergoes different types of chemistry during daytime and nighttime. In the daytime, nitrogen dioxide (NO_2) reacts with hydroxyl radicals (OH) to form nitric acid (HNO_3), which can be taken up into the particle phase, contributing to pNO_3^-. At nighttime, the reaction between NO_2 and O_3 forms gas-phase nitrate radicals (NO_3) and subsequently N_2O_5. The heterogeneous uptake and hydrolysis of N_2O_5 on particles produces pNO_3^- (see reactions (3)–(9) in Methods). In the presence of particulate chloride (pCl^-), multi-phase reactions of N_2O_5 will also form $ClNO_2$ and Cl_2, both of which are important nocturnal chlorine reservoirs. We measured the key nocturnal nitrogen species, N_2O_5 and $ClNO_2$, with an iodide-based chemical ionization mass spectrometer (see 'Measurements of N_2O_5, $ClNO_2$ and Cl_2' in Methods). They were substantially elevated during the lockdown period, especially during pollution episodes, with concentrations up to 2.0 ppb and 8.7 ppb, respectively (Extended Data Fig. 1). The increased levels of N_2O_5 are consistent with the low

https://doi.org/10.1038/s41561-023-01285-1

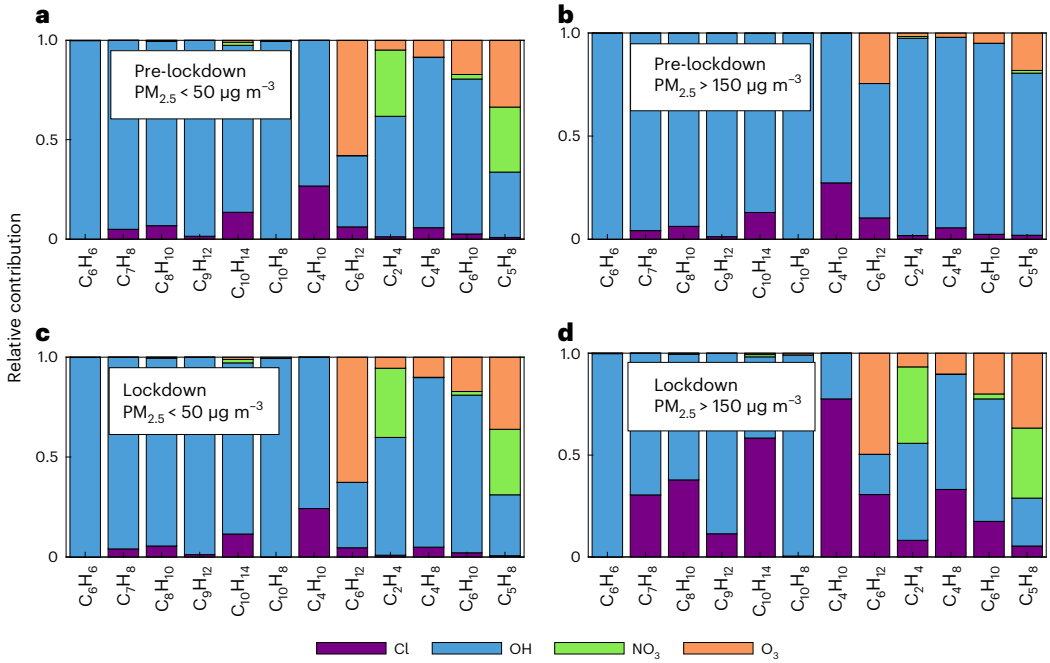

Fig. 3 | Relative contribution of VOC oxidation by different atmospheric oxidants, including Cl radicals, OH radicals, NO_3 radicals and O_3. a–d, The results under clean conditions during the pre-lockdown (**a**), polluted conditions during the pre-lockdown (**b**), clean conditions during the lockdown (**c**) and polluted conditions during the lockdown (**d**). The calculations of radical abundance and VOC oxidation rate are provided in the Methods.

NO and high O_3 during the lockdown period, while the elevated pNO_3^- and $ClNO_2$ (Fig. 1e) indicate that the N_2O_5 heterogeneous reactions on particle surfaces were also efficient in this period. In contrast, both N_2O_5 and $ClNO_2$ were suppressed during polluted conditions in the pre-lockdown period, due to the high nighttime NO (Fig. 1d). NO inhibits the formation of N_2O_5 by rapidly titrating NO_3 to NO_2 (see reaction (5) in Methods), and ultimately reduces the heterogeneous production of pNO_3^- and $ClNO_2$. It should be noted that considerable amounts of N_2O_5 (up to 1.1 ppb) and $ClNO_2$ (up to 2.8 ppb) were also observed in the pre-lockdown periods when NO was sufficiently low during clean nights (Extended Data Fig. 1). This is consistent with previous ground-based observations of N_2O_5 and $ClNO_2$ levels in urban Beijing[16–18]. Thus, based on our observations, we conclude that NO reductions can activate nighttime nitrogen chemistry, leading to the efficient formation of pNO_3^- and $ClNO_2$.

Substantial contribution of N_2O_5 to pNO_3^- production

To quantitatively evaluate the contribution of nocturnal nitrogen chemistry to pNO_3^- production, we examine the efficiency of N_2O_5 heterogeneous uptake, which is determined by the availability of particle surface area, the uptake coefficient of N_2O_5 on particle surfaces (γ) and the production yield of $ClNO_2$ (Φ). Detailed descriptions of the calculation are provided in the Methods. Previous studies have found that γ and Φ can vary drastically depending on the characteristics of particles, such as chemical composition, phase state and particle liquid water content[19–24]. We find that N_2O_5 heterogeneous uptake is primarily determined by ambient RH (Extended Data Fig. 3a); it is considerably more efficient at RH ≥ 60% (γ = 0.025) than at RH < 60% (γ = 0.005). The RH-dependence is consistent with our previous study at a rural site near Beijing[21]. At high RH, aerosols may contain more water and become less viscous, favouring the accommodation of N_2O_5 on the aerosol surface and ultimately facilitating the N_2O_5 heterogeneous reactions. We determine the yield of $ClNO_2$ during the lockdown period from the slope of $ClNO_2$ versus total nitrate[24]. The estimated Φ during the lockdown period is 0.45 (Extended Data Fig. 3b), which appears to be independent of the pCl^- concentration, probably because the chloride content is always sufficient and the aqueous-phase reaction of NO_2^+ and Cl^- is not the rate-limiting step for $ClNO_2$ formation.

Based on the derived N_2O_5 uptake coefficient and $ClNO_2$ yield, we calculate the nitrate formation from the N_2O_5 pathway, which is further compared to the contribution from the HNO_3 pathway. As shown in Fig. 2, the comparison is performed in four different scenarios: 'clean' ($PM_{2.5}$ < 50 μg m^{-3}) and 'polluted' ($PM_{2.5}$ > 150 μg m^{-3}) conditions during the pre-lockdown period (Fig. 2a,b) and during the lockdown period (Fig. 2c,d). Our calculations show that the HNO_3 pathway dominated pNO_3^- formation in both clean and polluted conditions during the pre-lockdown period, which is similar to the previous study of nitrate formation in Beijing during winter[25]. The minor contribution of the N_2O_5 pathway during the pre-lockdown period can be explained by the following considerations: (1) although a considerable amount of N_2O_5 was observed during clean conditions (Fig. 1d), the low N_2O_5 uptake coefficient due to low RH and low aerosol surface area limited the heterogeneous reactions of N_2O_5 and the formation of pNO_3^-; and (2) a low N_2O_5 concentration limited N_2O_5 heterogeneous reactions during polluted conditions (Fig. 1c). During the lockdown period, the contribution of N_2O_5 to pNO_3^- production was also limited during clean conditions (Fig. 2c) for the same reason as during the pre-lockdown period. However, under polluted conditions during the lockdown period, the co-existence of high N_2O_5 concentrations (Fig. 2d), high RH (thus high γ) and high aerosol surface area substantially enhanced the N_2O_5 heterogeneous reactions, which dominated pNO_3^- formation (58%). Our calculation is supported by pNO_3^- diurnal patterns observed in these four scenarios. As shown in Extended Data Fig. 4, pNO_3^- exhibits a daytime maximum in all scenarios other than the pollution condition during the lockdown period. In contrast, pNO_3^- shows a prominent increase during the night in the pollution condition of the lockdown period, confirming our former calculations that the N_2O_5 heterogeneous reactions become a dominant source of pNO_3^-. Aside from this, daytime pNO_3^- shows the steepest increase during polluted conditions of the pre-lockdown period, which is consistent with the highest HNO_3^--driven pNO_3^- formation rate (Fig. 2b).

https://doi.org/10.1038/s41561-023-01285-1

The exact contribution of the N_2O_5 pathway and HNO_3 pathway calculated based on in situ measurements are quantitatively valid on the ground level at this location. However, these contributions may vary in different locations depending on atmospheric conditions, particularly the concentrations of NO, NO_2 and O_3. For example, using data from three other Chinese megacities—Shanghai, Nanjing and Shijiazhuang—we observe that while the trends in NO, NO_2 and O_3 are similar, their magnitudes of changes are different (see Extended Data Fig. 5). We further compare the fractional contribution of pNO_3^- to $PM_{2.5}$ and the effective conversion efficiency of NO_2 to pNO_3^- during the pre-lockdown and lockdown periods in these cities. Associated with the enhanced nocturnal nitrogen chemistry, the conversion efficiency of NO_2 to pNO_3^- is enhanced by a factor of 3–5. This can at least partially explain the increased contribution of pNO_3^- to $PM_{2.5}$ despite the substantial reduction in NO_x concentration. These findings suggest that although the exact magnitude of the enhancement may differ among locations, the enhanced nocturnal nitrogen chemistry is a regional phenomenon over a large area in China. Moreover, the contribution of the N_2O_5 pathway to pNO_3^- formation is also subject to the uncounted influence of the mixing of the boundary layer. During the pre-lockdown period, the N_2O_5 pathway could have been more critical in the residual layer where NO concentration might be low enough to allow for efficient N_2O_5 and pNO_3^- formation. This could contribute to ground-level pNO_3^- concentration through convection when the mixing layer builds up the following morning[26,27]. In contrast, the N_2O_5 pathway could have been less efficient in the residual layer than at the ground level, as the production rate of NO_3 and N_2O_5 (see reaction (3) in Methods) is probably lower in the former. This is qualitatively illustrated by our additional three-dimensional modelling (WRF-Chem) focusing on vertical profiles of NO, NO_2, O_3 and pNO_3^- production rate (Supplementary Information).

Formation of OOM-driven Cl-radical-initiated VOC oxidation

We now turn to an assessment of the consequences of nocturnal nitrogen chemistry on the atmospheric oxidation capacity during the following day. As shown in Fig. 1, the nocturnal chlorine reservoir species, $ClNO_2$, was greatly enhanced during the lockdown period. This was accompanied by an increase in molecular chlorine (Cl_2; Extended Data Fig. 6), most probably a co-product of $ClNO_2$ production from N_2O_5 uptake on acidic aerosols[28,29]. At sunrise, upon photolysis, these chlorine species liberate highly reactive chlorine atoms (Cl), an important radical that can oxidize some volatile organic compound (VOC) species more rapidly than the OH-initiated oxidation chemistry (Supplementary Table 1). To quantify the contribution of Cl radicals to the atmospheric oxidative capacity, we use a box model with implemented chlorine chemistry (see 'Estimation of the Cl radical concentration and VOC oxidation rates' in Methods) to estimate the Cl concentration during the measurement period (Extended Data Fig. 7). Then, we calculate the turnover rates of numerous VOCs by OH radicals, Cl radicals, NO_3 radicals and O_3 separately and compare their contribution under different $PM_{2.5}$ levels as before (that is, $PM_{2.5} < 50\ \mu g\ m^{-3}$ and $PM_{2.5} > 150\ \mu g\ m^{-3}$).

As shown in Fig. 3, the oxidation of aromatic VOCs is initiated by OH radicals in most cases, consistent with the general understanding that OH radicals are the most important oxidant for VOC degradation. However, the contribution of Cl radicals to the oxidation of aromatic VOCs is crucial under polluted conditions during the lockdown periods (Fig. 3d). The crucial role of Cl radicals in VOC oxidation is further connected to the formation of oxygenated organic molecules (OOMs), which we measured with an atmospheric pressure interface time-of-flight mass spectrometer equipped with nitrate chemical ionization sources (nitrate CI-APi-TOF; see 'Measurements of sulfuric acid and OOMs' in Methods) and classified based on our recently developed classification workflow[30]. As shown in Extended Data Fig. 8, the OOM

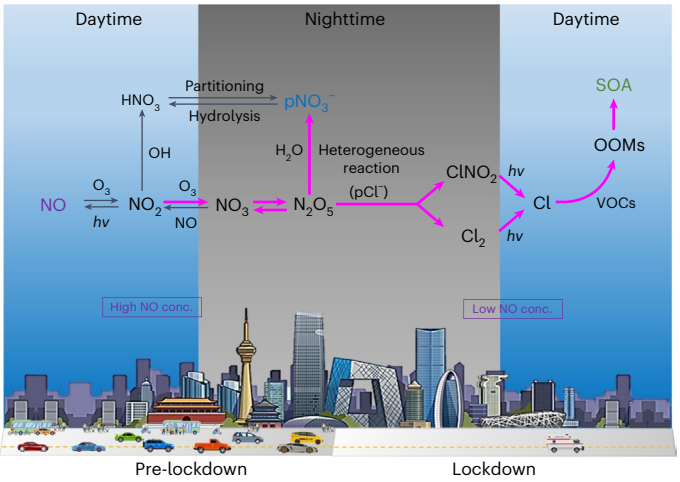

Fig. 4 | The amplified nocturnal nitrogen chemistry and impacts on air quality. A simplified schematic diagram showing the nocturnal formation of N_2O_5. N_2O_5 undergoes heterogeneous uptake on aerosol during nighttime to form $ClNO_2$, Cl_2 and pNO_3^-. At sunrise, these chlorine reservoirs will be photolysed to the Cl radical, which can oxidize VOC to produce OOMs—the essential precursors of SOA. Typically, the NO concentration is high in the pre-lockdown period, restricting the formation of N_2O_5 and its heterogeneous processes. During the lockdown period, NO concentration was substantially decreased, enhancing the formation of N_2O_5, ultimately leading to an increase in pNO_3^- and OOMs. Note that the thick pink arrows represent the reactions that are greatly enhanced during the lockdown period.

yield of aromatic VOC oxidation initiated by Cl is likely to be more than two-fold higher than that in OH-initiated oxidation. Considering the rapid VOC oxidation and the high OOM yield altogether, the aromatic VOC oxidation initiated by Cl radicals can have a roughly equal contribution to that initiated by OH radicals under the polluted conditions in the lockdown period. In addition to the oxidation of aromatics, Cl radicals are consistently important for the oxidation of alkanes, which become dominant when nocturnal nitrogen chemistry is amplified (Fig. 3d). The substantial contribution to the formation of alkane-originated OOMs is thus expected. Altogether, we conclude that the amplified nocturnal nitrogen chemistry leads to a substantial enhancement of OOM formation, and consequently, SOA formation.

The increasing importance of nocturnal nitrogen chemistry

In summary, as illustrated in Fig. 4, we provide direct evidence that the substantial reductions in NO_x emissions can activate nocturnal nitrogen chemistry during severe pollution episodes, which in turn drives haze formation. Using our observations during the COVID-19 lockdown, we illustrate two prominent effects of nocturnal nitrogen chemistry in haze formation. First, heterogeneous reactions of N_2O_5 dominated nitrate formation under polluted conditions during the lockdown period, leading to a higher-than-normal pNO_3^- contribution to the overall $PM_{2.5}$ loading despite the dramatic NO_x reduction. Given abundant gas-phase NH_3 in China, the enhanced pNO_3^- formation also led to additional pNH_4^+ production. In addition, the high fraction of pNO_3^- can increase aerosol hygroscopicity and liquid water content of aerosols, which might facilitate the aqueous- and multi-phase chemistry that is important for haze formation[31,32]. Second, $ClNO_2$ and Cl_2 formed at night released abundant Cl radicals into the atmosphere via photolysis the next morning, contributing appreciably to the oxidation of monocyclic aromatic VOCs and alkanes. Those aromatic and aliphatic OOMs are known to be major contributors to the formation of SOA in China's megacities[30], and therefore, the amplified nocturnal nitrogen chemistry is essential for the enhanced SOA formation (Fig. 1).

Nocturnal nitrogen chemistry during the lockdown period was entirely different from normal conditions (that is, the pre-lockdown period) in Beijing. Nevertheless, it may vividly depict future scenarios if NO_x emissions undergo stringent control without simultaneous control of O_3, because activated nighttime nitrogen chemistry is essentially caused by the removal of most NO by excess O_3 during the night. In other words, nighttime NO concentration is the key factor that determines whether the nocturnal nitrogen chemistry is important. In a recent study, night oxidation regulated by nocturnal nitrogen chemistry was shown to increase in China but decreased across the globe on average[33]. However, when concerning the nocturnal nitrogen chemistry under relatively polluted conditions, we find that NO concentrations in all urban or suburban environments in the world remain high enough to inhibit efficient nocturnal nitrogen chemistry (Extended Data Fig. 9). Given that NO_x has been continuously declining globally[34–38], it can be anticipated that the suppression by NO will diminish gradually, and nocturnal nitrogen chemistry will be enhanced. Therefore, our results suggest that nocturnal nitrogen chemistry is gaining increasing importance in urban and suburban areas globally.

From a pollution control point of view, mitigating $PM_{2.5}$ pollution is the principal aim for North China. Our findings highlight that if O_3 production cannot be controlled by simultaneously modulating VOC and NO_x emission, amplified nighttime nitrogen chemistry can cause sustained haze pollution. It is common to consider O_3 formation and control in terms of the VOC:NO_x ratio[39,40]. However, our findings emphasize the central role of nocturnal NO, especially when assessing the importance of nocturnal nitrogen chemistry in the coupled O_3 and $PM_{2.5}$ pollution. Although air pollution control strategies may vary from location to location, the complex influence of NO, NO_2, VOC and O_3 on nighttime chemistry needs to be given more attention in formulating future emission control strategies.

Online content

Any methods, additional references, Nature Portfolio reporting summaries, source data, extended data, supplementary information, acknowledgements, peer review information; details of author contributions and competing interests; and statements of data and code availability are available at https://doi.org/10.1038/s41561-023-01285-1.

References

1. Lelieveld, J., Evans, J. S., Fnais, M., Giannadaki, D. & Pozzer, A. The contribution of outdoor air pollution sources to premature mortality on a global scale. *Nature* **525**, 367–371 (2015).
2. Zhang, L. et al. Air pollution-induced missed abortion risk for pregnancies. *Nat. Sustain.* **2**, 1011–1017 (2019).
3. Cai, W. et al. The 2020 China report of the *Lancet* Countdown on health and climate change. *Lancet Public Health* **6**, e64–e81 (2021).
4. Wang, Y. et al. Contrasting trends of $PM_{2.5}$ and surface-ozone concentrations in China from 2013 to 2017. *Natl Sci. Rev.* **7**, 1331–1339 (2020).
5. Cooper, M. J. et al. Global fine-scale changes in ambient NO_2 during COVID-19 lockdowns. *Nature* **601**, 380–387 (2022).
6. Shi, Z. et al. Abrupt but smaller than expected changes in surface air quality attributable to COVID-19 lockdowns. *Sci. Adv.* **7**, eabd6696 (2021).
7. Miyazaki, K. et al. Global tropospheric ozone responses to reduced NO_x emissions linked to the COVID-19 worldwide lockdowns. *Sci. Adv.* **7**, eabf7460 (2021).
8. Venter, Z. S., Aunan, K., Chowdhury, S. & Lelieveld, J. COVID-19 lockdowns cause global air pollution declines. *Proc. Natl Acad. Sci. USA* **117**, 18984–18990 (2020).
9. Chang, Y. et al. Puzzling haze events in china during the coronavirus (COVID-19) shutdown. *Geophys. Res. Lett.* **47**, e2020GL088533 (2020).
10. Sun, Y. et al. A chemical cocktail during the COVID-19 outbreak in Beijing, China: insights from six-year aerosol particle composition measurements during the Chinese New Year holiday. *Sci. Total Environ.* **742**, 140739 (2020).
11. Huang, X. et al. Enhanced secondary pollution offset reduction of primary emissions during COVID-19 lockdown in China. *Natl Sci. Rev.* **8**, nwaa137 (2021).
12. Shi, X. & Brasseur, G. P. The response in air quality to the reduction of Chinese economic activities during the COVID-19 outbreak. *Geophys. Res. Lett.* **47**, e2020GL088070 (2020).
13. Huang, G. & Sun, K. Non-negligible impacts of clean air regulations on the reduction of tropospheric NO_2 over East China during the COVID-19 pandemic observed by OMI and TROPOMI. *Sci. Total Environ.* **745**, 141023 (2020).
14. Le, T. et al. Unexpected air pollution with marked emission reductions during the COVID-19 outbreak in China. *Science* **369**, 702–706 (2020).
15. Wang, P., Chen, K., Zhu, S., Wang, P. & Zhang, H. Severe air pollution events not avoided by reduced anthropogenic activities during COVID-19 outbreak. *Resour. Conserv. Recycl.* **158**, 104814 (2020).
16. Wang, H. et al. High N_2O_5 concentrations observed in urban Beijing: implications of a large nitrate formation pathway. *Environ. Sci. Technol. Lett.* **4**, 416–420 (2017).
17. Zhou, W. et al. Production of N_2O_5 and $ClNO_2$ in summer in urban Beijing, China. *Atmos. Chem. Phys.* **18**, 11581–11597 (2018).
18. Xia, M. et al. Winter $ClNO_2$ formation in the region of fresh anthropogenic emissions: seasonal variability and insights into daytime peaks in northern China. *Atmos. Chem. Phys.* **21**, 15985–16000 (2021).
19. Bertram, T. & Thornton, J. Toward a general parameterization of N_2O_5 reactivity on aqueous particles: the competing effects of particle liquid water, nitrate and chloride. *Atmos. Chem. Phys.* **9**, 8351–8363 (2009).
20. Bertram, T. H. et al. Direct observations of N_2O_5 reactivity on ambient aerosol particles. *Geophys. Res. Lett.* **36**, L19803 (2009).
21. Tham, Y. J. et al. Heterogeneous N_2O_5 uptake coefficient and production yield of $ClNO_2$ in polluted northern China: roles of aerosol water content and chemical composition. *Atmos. Chem. Phys.* **18**, 13155–13171 (2018).
22. Galib, M. & Limmer, D. T. Reactive uptake of N_2O_5 by atmospheric aerosol is dominated by interfacial processes. *Science* **371**, 921–925 (2021).
23. Jahl, L. G., Bowers, B. B., Jahn, L. G., Thornton, J. A. & Sullivan, R. C. Response of the reaction probability of N_2O_5 with authentic biomass-burning aerosol to high relative humidity. *ACS Earth Space Chem.* **5**, 2587–2598 (2021).
24. Phillips, G. J. et al. Estimating N_2O_5 uptake coefficients using ambient measurements of NO_3, N_2O_5, $ClNO_2$ and particle-phase nitrate. *Atmos. Chem. Phys.* **16**, 13231–13249 (2016).
25. Chen, X. et al. Field determination of nitrate formation pathway in winter Beijing. *Environ. Sci. Technol.* **54**, 9243–9253 (2020).
26. Wang, H. et al. Fast particulate nitrate formation via N_2O_5 uptake aloft in winter in Beijing. *Atmos. Chem. Phys.* **18**, 10483–10495 (2018).
27. Tham, Y. J., Wang, Z., Li, Q., Yun, H. & Wang, T. Significant concentrations of nitryl chloride sustained in the morning: investigations of the causes and impacts on ozone production in a polluted region of northern China. *Atmos. Chem. Phys.* **16**, 14959–14977 (2016).
28. Roberts, J. M., Osthoff, H. D., Brown, S. S. & Ravishankara, A. R. N_2O_5 oxidizes chloride to Cl_2 in acidic atmospheric aerosol. *Science* **321**, 1059 (2008).

29. Xia, M. et al. Significant production of $ClNO_2$ and possible source of Cl_2 from N_2O_5 uptake at a suburban site in eastern China. *Atmos. Chem. Phys.* **20**, 6147–6158 (2020).
30. Nie, W. et al. Secondary organic aerosol formed by condensing anthropogenic vapours over China's megacities. *Nat. Geosci.* **15**, 255–261 (2022).
31. Cheng, Y. et al. Reactive nitrogen chemistry in aerosol water as a source of sulfate during haze events in China. *Sci. Adv.* **2**, e1601530 (2016).
32. Liu, T. & Abbatt, J. P. D. Oxidation of sulfur dioxide by nitrogen dioxide accelerated at the interface of deliquesced aerosol particles. *Nat. Chem.* **13**, 1173–1177 (2021).
33. Wang, H. et al. Increased night-time oxidation over China despite widespread decrease across the globe. *Nat. Geosci.* **16**, 217–223 (2023).
34. Russell, A. R., Valin, L. C. & Cohen, R. C. Trends in OMI NO_2 observations over the United States: effects of emission control technology and the economic recession. *Atmos. Chem. Phys.* **12**, 12197–12209 (2012).
35. Praske, E. et al. Atmospheric autoxidation is increasingly important in urban and suburban North America. *Proc. Natl Acad. Sci. USA* **115**, 64–69 (2018).
36. Chan, K. L., Khorsandi, E., Liu, S., Baier, F. & Valks, P. Estimation of surface NO_2 concentrations over germany from TROPOMI satellite observations using a machine learning method. *Remote Sens.* **13**, 969 (2021).
37. Hu, M. et al. Estimation and spatiotemporal analysis of NO_2 pollution in East Asia during 2001–2016. *J. Geophys. Res. Atmos.* **127**, e2021JD035129 (2022).
38. Zhou, M. et al. Elevated formation of particulate nitrate from N_2O_5 hydrolysis in the Yangtze River Delta region from 2011 to 2019. *Geophys. Res. Lett.* **49**, e2021GL097393 (2022).
39. Sillman, S. The relation between ozone, NO_x and hydrocarbons in urban and polluted rural environments. *Atmos. Environ.* **33**, 1821–1845 (1999).
40. He, Z. et al. Contributions of different anthropogenic volatile organic compound sources to ozone formation at a receptor site in the Pearl River Delta region and its policy implications. *Atmos. Chem. Phys.* **19**, 8801–8816 (2019).

[1]Aerosol and Haze Laboratory, Beijing Advanced Innovation Center for Soft Matter Science and Engineering, Beijing University of Chemical Technology, Beijing, China. [2]Joint International Research Laboratory of Atmospheric and Earth System Science, School of Atmospheric Sciences, Nanjing University, Nanjing, China. [3]Institute for Atmospheric and Earth System Research/Physics, Faculty of Science, University of Helsinki, Helsinki, Finland. [4]School of Marine Sciences, Sun Yat-sen University, Zhuhai, China. [5]Department of Civil and Environmental Engineering, The Hong Kong Polytechnic University, Hong Kong, China. [6]School of Atmospheric Sciences, Sun Yat-sen University, Zhuhai, China. [7]State Key Joint Laboratory of Environment Simulation and Pollution Control, School of Environment, Tsinghua University, Beijing, China. [8]Department of Atmospheric Chemistry and Climate, Institute of Physical Chemistry Blas Cabrera, CSIC, Madrid, Spain. [9]State Key Laboratory of Severe Weather & Key Laboratory of Atmospheric Chemistry of China Meteorological Administration (CMA), Chinese Academy of Meteorological Sciences, Beijing, China. [10]Indian Institute of Tropical Meteorology, Ministry of Earth Sciences, Pune, India. [11]State Environmental Protection Key Laboratory of Formation and Prevention of Urban Air Pollution Complex, Shanghai Academy of Environmental Sciences, Shanghai, China. [12]Division of Environment and Sustainability, The Hong Kong University of Science and Technology, Hong Kong, China. [13]Institute of Atmospheric Physics, Chinese Academy of Sciences, Beijing, China. [14]Aerodyne Research Inc., Billerica, MA, USA. [15]Center for Atmospheric Particle Studies, Carnegie Mellon University, Pittsburgh, PA, USA. [16]These authors contributed equally: Chao Yan, Yee Jun Tham. ✉e-mail: thamyj@mail.sysu.edu.cn; dingaj@nju.edu.cn; markku.kulmala@helsinki.fi

Methods

Measurements

Sampling site description. The measurements were conducted at the newly established Aerosol and Haze Laboratory of the Beijing University of Chemical Technology (AHL-BUCT; 39° 56′ 31″ N, 116° 17′ 50″ E). All instruments were housed in the laboratory located on the fifth floor of the main teaching building, about 18 m above the ground surface. The building is surrounded by main roads, and residential and commercial areas, therefore it is a typical urban observation station. A detailed description of this station can be found elsewhere[41–44].

Measurement of particle number size distribution. The number size distributions of particles in the size range of 1 nm–10 μm were measured by a diethylene glycol scanning mobility particle spectrometer (DEG-SMPS, 1–7.5 nm)[45] and a particle size distribution system (PSD, 3 nm–10 μm)[46]. The inlet flow of DEG-SMPS was sampled from the core of the total flow at the exit of a ~1.2 m sampling line to improve the sampling efficiency of nanoparticles[47,48]. The effective aerosol flow rate of the DEG-SMPS was about 0.25 l min^{-1}. The sampling line of the PSD was 3 m long from the rooftop, with a PM_{10} cyclone as the inlet. Other configurations of the instruments were similar to those used in previous campaigns[49]. During the data inversion procedure, correlations of particle diffusion loss, bipolar charging efficiency, multiple charge and detection efficiency are accounted for.

Measurements of N_2O_5, $ClNO_2$ and Cl_2. As the core observation of this study, N_2O_5, $ClNO_2$ and Cl_2 were measured with a high-resolution time-of-fight (TOF) chemical ionization mass spectrometer using iodide as the reagent ion (I-CIMS)[50]. The instrument was operated with a Filter Inlet for Gases and AEROsols (FIGAERO) inlet[51], where measurement was alternately switched between gas phase and aerosol phase. A 1.5-m-long Teflon tubing (6.35 mm outer diameter) was used as the sampling inlet. The total sampling flow was set at a rate of 8 l min^{-1}, out of which only 1.5 l min^{-1} was directed into the CIMS instrument, while the rest was exhausted. The total retention time in the inlet was calculated to be approximately 140 ms.

The calibration methods and setup for N_2O_5 and $ClNO_2$ have been described in our previous study[52,53]. Briefly, N_2O_5 was produced by mixing O_3 with NO_2 in excess. The concentration of produced N_2O_5 was determined by the changes in NO_2 concentration before and after reacting O_3 with NO_2. A known amount of N_2O_5 was directed through a Teflon reactor filled with deliquesced sodium chloride (NaCl) slurry to produce $ClNO_2$. The concentration of the $ClNO_2$ was determined via the amount of N_2O_5 loss through the NaCl-filled reactor compared to an empty reactor with the assumption of 100% conversion efficiency. As for the Cl_2 calibration, a Cl_2 permeation tube (in a permeation oven set at 40 °C; VICI Metronic) was used to produce Cl_2 gas standard for dilution in various N_2 flow rates to obtain different levels of Cl_2. The permeation rate of Cl_2 (225 ± 56 ng min^{-1}) was quantified by chemical titration and ultraviolet (UV) spectrophotometry[54]. Supplementary Fig. 2 shows the calibration results of N_2O_5, $ClNO_2$ and Cl_2 for the I-CIMS. The instrument sensitivities to N_2O_5, $ClNO_2$ and Cl_2 were determined under different RH at room temperature (22.5 ± 0.1 °C). We converted RH to absolute water concentration and then fitted the water-dependent sensitivities using empirical equations to apply the calibration factor to ambient measurement. The water-dependent calibration coefficients of N_2O_5, $ClNO_2$ and Cl_2 are shown in Supplementary Fig. 2.

Measurements of sulfuric acid and OOMs. Sulfuric acid (H_2SO_4) and OOMs were measured by nitrate CI-APi-TOF (Aerodyne Research)[55]. To quantify H_2SO_4 concentration, this instrument was calibrated with known concentrations of gaseous sulfuric acid produced by the reaction of SO_2 and OH radicals formed by ultraviolet photolysis of water vapour[56]. A calibration coefficient of 6.57×10^9 cm^{-3} normalized counts per second was obtained after taking the inlet sampling loss into account. In the daytime, because the primary source and loss terms of H_2SO_4 is the reaction between SO_2 and OH radical and the condensation sink (CS), we estimated the concentration of OH radicals from measured H_2SO_4 concentration as below:

$$[\mathrm{OH}] = \frac{[\mathrm{H_2SO_4}] \times \mathrm{CS}}{k(T) \times [\mathrm{SO_2}]} \quad (1)$$

where [OH], $[H_2SO_4]$ and $[SO_2]$ are the concentrations of OH radical, H_2SO_4 and SO_2, respectively, k denotes the reaction rate constant between OH radical and SO_2, that is, 1.3×10^{-12} $(T/300)^{-0.7}$ cm^3 s^{-1} (ref. 57), where T denotes the absolute temperature, and CS represents the first-order loss rate of H_2SO_4 onto particle surfaces and was calculated using the following equation[58]:

$$\mathrm{CS} = 2\pi D_\mathrm{v} \int_0^{d_\mathrm{p,max}} d_\mathrm{p} \beta n(d_\mathrm{p}) d d_\mathrm{p} \quad (2)$$

Here, d_p is the particle diameter measured by the combination of DEG-SMPS and PSD; β is the dimensionless transitional correction factor for mass flux; $n(d_p)$ is the number concentration of particles of diameter d_p; and D_v is the diffusion coefficient of H_2SO_4. We show the estimated OH concentration in Extended Data Fig. 7. The daytime mean concentration of OH throughout the period is calculated to be 1.7×10^6 cm^{-3}, which is about 30% lower than measured OH concentrations for the same season reported previously in Beijing[59].

Estimation of OOM concentration included two steps. First, a mass-dependent transmission correction was performed. This transmission bias is determined by comparing the decrease in the primary ion signals and the increase in signals from added perfluorinated acids[60]. Second, we applied the calibration coefficient determined for sulfuric acid to estimate the OOM concentration. However, a recent study has pointed out that this assumption does not hold for less oxidized organic compounds[61], as nitrate ions do not ionize some molecules as efficiently as H_2SO_4. Thus, the reported concentration of oxidized organic vapours in this study is rather a lower limit, especially for less oxidized compounds. All detected OOMs were classified to their potential sources, including aromatic-OOMs, aliphatic-OOMs, monoterpene-OOMs and isoprene-OOMs. This was done with the recently developed workflow, which has been explained in detail elsewhere[30].

Measurement of aerosol chemical composition. The mass concentrations of non-refractory $PM_{2.5}$ (including organic aerosol, pSO_4^{2-}, pNO_3^-, pNH_4^+ and pCl^-) were obtained with a TOF Aerosol Chemical Speciation Monitor (TOF-ACSM, equipped with a standard vaporizer)[62] and were corrected for the CO_2/NO_3 artefact outlined in ref. 63. The TOF-ACSM was regularly calibrated (ionization efficiency) and relative ionization efficiency of pNH_4^+ (3.76), pSO_4^{2-} (0.88) and pCl^- (1.5) were determined experimentally by using nebulized aqueous solutions of pure NH_4NO_3, pure $(NH_4)_2SO_4$ and pure NH_4Cl into the TOF-ACSM. Default relative ionization efficiency values were used for organic aerosol (1.4) and pNO_3^- (1.05). Chemical composition-dependent collection efficiency[64] was also applied.

Measurement of VOCs. VOCs were detected by proton transfer reaction TOF mass spectrometry (PTR-TOF-MS 8000, IONICON) with a hydronium ion (H_3O^+) source. VOCs undergo proton transfer reactions with H_3O^+, producing $(VOC)H^+$ ions detected by the mass spectrometer. Multipoint calibrations were performed using TO-15 calibration gas standards before and after the experiment. A total of 30 out of 65 VOC compounds could be detected by the PTR-TOF-MS, for which calibrated results were directly obtained by using the linear regression multipoint calibrations, yielding a linear correlation coefficient (R) above 0.99. VOC data were acquired at 10 s time resolution and averaged into hourly data for analysis.

Other ancillary measurements. Meteorological parameters are measured with a weather station (AWS310, Vaisala) located on the rooftop of the building. These parameters include the ambient temperature, RH, pressure, visibility, UVB radiation, and horizontal wind speed and direction. Additionally, the atmospheric boundary layer height is retrieved from ceilometer measurements of the optical backscattering. Trace gas concentrations of CO, SO_2, NO_x and O_3 are monitored using four Thermo Environmental Instruments (models 48i, 43i-TLE, 42i and 49i, respectively). These gases' pollutants are sampled using a 3 m tube from the roof. To reduce the sampling loss of these gases, the inlet tube is heated to 313 K. Calibrations of these instruments are performed bi-weekly using the standard gases of known concentrations.

Calculation of N_2O_5 uptake coefficient and nitrate formation rate

The nocturnal nitrogen chemistry mainly includes the following reactions:

$$NO_2 + O_3 \xrightarrow{k_1} NO_3 + O_2 \quad (3)$$

$$NO_3 + VOC \xrightarrow{k_2} \text{Products} \quad (4)$$

$$NO_3 + NO \xrightarrow{k_3} 2NO_2 \quad (5)$$

$$NO_2 + NO_3 + M \xrightarrow{k_4} N_2O_5 + M \quad (6)$$

$$N_2O_5 + M \xrightarrow{k_5} NO_2 + NO_3 + M \quad (7)$$

$$N_2O_5 + H_2O(s) + Cl^- \xrightarrow{k_{N_2O_5}} (2-\Phi)pNO_3^- + \Phi\, ClNO_2 \quad (8)$$

$$ClNO_2 + h\nu \rightarrow Cl\cdot + NO_2 \quad (9)$$

Once NO_3 radical is formed via the reaction between NO_2 and O_3 (reaction (3)), it quickly achieves thermal equilibrium with N_2O_5 in the presence of NO_2 (reactions (6) and (7)), which can be described as:

$$[N_2O_5] = K_{eq}[NO_2][NO_3], K_{eq} = k_4/k_5 \quad (10)$$

Here, K_{eq} is the equilibrium constant determined as the ratio of k_4 to k_5, which is $1.9 \times 10^{-12}\,(T/300)^{0.2}$ cm^3 molecule^{-1} s^{-1} (ref. 65) and $9.7 \times 10^{14}\,(T/300)^{0.1} \exp^{(-11080/T)}$ s^{-1} (ref. 66), respectively. With the known $K_{eq}[NO_2]$, we can then calculate the NO_3 radical concentration based on the measured N_2O_5 concentration.

Brown et al. proposed a statistical method to derive the steady-state loss rates of NO_3 and N_2O_5, based on the field measured NO_2, O_3, NO_3 and N_2O_5 (ref. 67). Briefly, if the NO_3 and N_2O_5 are both in a steady-state condition, for which their total formation rates and total loss rates should be roughly equivalent and much larger than the net change rates, the equation can be shown as below:

$$k_1[NO_2][O_3] = k_{NO_3}[NO_3] + k_{N_2O_5}[N_2O_5] \quad (11)$$

where k_{NO3} and k_{N2O5} denote the first-order total loss rates for NO_3 and N_2O_5, respectively. The main contributors of k_{NO3} include the reactions with NO and some biogenic VOCs, such as isoprene and monoterpene. In most urban environments, the reaction between NO_3 and NO is the overwhelming term in k_{NO3} due to the high reaction rate and high NO condensation. Take Beijing as an example, ref. 16 reported that the total loss rate of NO_3 due to reactions with VOCs in summer was in the range of 0.001–0.057 s^{-1}, which is equivalent to the loss to 1.5–87 ppt of NO.

The loss rate of N_2O_5 (k_{N2O5}) is solely due to the uptake on the particle surface, which can be expressed as:

$$k_{N_2O_5} = \frac{1}{4}cS\gamma \quad (12)$$

where c is the mean molecular speed of N_2O_5, which is 240 m s^{-1}, S is the concentration of total particle surface area, which can be calculated based on the particle number size distribution, and γ is the uptake coefficient of N_2O_5.

When the steady-state assumption holds, the lifetime of NO_3, $\tau(NO_3)$, can be calculated by equation (13) shown below, and the inverse lifetime of NO_3 ($\tau(NO_3)^{-1}$) can be expressed by equation (14):

$$\tau(NO_3) = \frac{[NO_3]}{k_1[NO_2][O_3]} = \frac{[NO_3]}{k_{NO_3}[NO_3] + k_{N_2O_5}[N_2O_5]} \quad (13)$$

$$\tau(NO_3)^{-1} = k_{NO_3} = K_{eq}[NO_2]k_{N_2O_5} = k_{NO_3} + \frac{1}{4}cS\gamma K_{eq}[NO_2] \quad (14)$$

From equation (14), the inverse of NO_3 lifetime can be described as a linear function of $\frac{1}{4}cSK_{eq}[NO_2]$. $\tau(NO_3)^{-1}$ and $\frac{1}{4}cSK_{eq}[NO_2]$ can be obtained from the measurement, and k_{NO3} and γ were determined as the intercept and the slope of the linear regression, respectively (see Extended Data Fig. 3a). After obtaining γ (and, in turn, k_{N2O5}) and the production yield of $ClNO_2$ (ϕ; see Extended Data Fig. 3b), the formation rate of pNO_3^- through the N_2O_5 heterogeneous reactions can be calculated based on reaction (8).

In the calculation, there are two points to be noted. First, the steady-state assumption of NO_3 and N_2O_5 may not hold if there is strong NO emission nearby. This was very common in the pre-lockdown period with large on-road traffic volume, but in the lockdown period, NO_3 and N_2O_5 were most probably always in a steady state because the fresh NO emission was almost completely removed. Second, the measured particle number size distribution is based on the dry particle size, so the parameter S may not fully characterize the actual particle surface under high RH conditions. Without real-time measurements of particle hygroscopicity and growth factor, we could not calculate S based on the wet size of particles. Hence, the γ derived in this study suffers from a certain degree of over-estimation. Nevertheless, because the N_2O_5 heterogeneous reactions in our case were in a γ-insensitive regime[26], in which the product of γ and S determines the overall uptake rate of N_2O_5, the under-estimation of S and the corresponding over-estimation of γ should have little influence on our calculation of pNO_3^- formation rate. Overall, this steady-state calculation has been commonly used in determining the pNO_3^- under low-NO conditions (for example, refs. 16,67–69), although using the isotopic method may shed a different light on pNO_3^- formation[70,71].

Estimation of the Cl radical concentration and VOC oxidation rates

A chemical box model, the Framework for 0-D Atmospheric Modeling (F0AM version 4.0.2)[72], is applied here to estimate the ambient mixing ratio of the Cl atom. The F0AM model has been used in previous studies to evaluate the role of reactive halogens in the troposphere[73,74]. The model contains the main production and loss processes of the Cl atom, including the photolysis of reactive chlorine species ($ClNO_2$, Cl_2, HOCl), the reactions of Cl with O_3 and various VOCs, and so on. The mixing ratio of Cl atoms is simulated by applying Master Chemical Mechanism (MCM) v3.3.1 (http://mcm.york.ac.uk) and a chlorine chemistry module[75]. Dilution and deposition are calculated as first-order loss reactions for each species.

Here, we conducted one simulation, which is constrained with the observational data, including the main Cl atom precursors ($ClNO_2$ and Cl_2), the main loss channels (O_3, CH_4 and VOCs) and other relevant

species (N_2O_5, HONO, SO_2, NO, NO_2, CO). The observed data are interpolated to the simulation time step (5 min) before being input to the model. The simulation period is from 26 December 2019 to 15 February 2020, covering both the pre-lockdown and lockdown periods in Beijing. Simulation of the first day (that is, 26 December 2019) was repeated three times to stabilize intermediates, and only results from the last time are used for further analysis.

The output concentration of Cl radicals, together with calculated OH, NO_3 (measured), and O_3 (measured) concentrations, were used to calculate the VOCs' oxidation rate (Fig. 3) with equation (15):

$$\mathrm{VOC_i\ oxidation\ rate} = \sum k_{\mathrm{VOC}_{ij}}[\mathrm{VOC_i}][X_j] \quad (15)$$

Here, VOC_i represents the individual VOC concentration, and X_j is the concentration of oxidants, including Cl, OH, NO_3 and O_3. The reaction rate coefficient ($k_{\mathrm{VOC}_{ij}}$) was adopted from the International Union of Pure and Applied Chemistry (IUPAC) kinetic database[57]. Note that some VOC species from our measurements may contain different isomers, but we only choose a single isomer for the calculation as we cannot separate them. For example, C_8H_{10} is presumed to be ethylbenzene, and C_9H_{12} as 1,3,5-trimethylbenzene. Supplementary Table 1 shows the details of the VOC and its reaction rate coefficient used in this calculation. Owing to the full availability of data, the VOC oxidation rate was calculated from 26 December 2019 until 15 February 2020.

Calculation of Δ[aromatic-OOMs] and the yield-weighted reacted aromatics

Based on the measurement of OOMs by the nitrate CIMS and the recently developed workflow[30], we calculate the source-classified OOMs, including aromatic-OOMs, aliphatic-OOMs, isoprene-OOMs and monoterpene-OOMs. It has been shown in our previous study that aromatic-OOMs and aliphatic-OOMs are the major OOM components[30]. We choose aromatic-OOMs to demonstrate the importance of Cl-initiate oxidation of aromatic hydrocarbons. In terms of OOM composition, aliphatic-OOMs are about equally as important as aromatic-OOMs[30]. However, because the long-chain alkanes cannot be well quantified by the PTR-TOF, we are not able to build quantitative connections between the VOC oxidation and the product concentration.

As illustrated in Supplementary Fig. 3, we calculate Δ[aromatic-OOMs] on a daily basis by determining the minima and maxima aromatic-OOM concentrations and their corresponding time windows (Δt). Our results show that the minimal and maximal aromatic-OOM concentrations are usually observed at 7:00–8:00 a.m. and 1:00–2:00 p.m., respectively, suggesting that the formation of aromatic-OOMs is driven by photochemical oxidation. Then we calculate the total reacted aromatics within these time windows, according to the calculated VOC oxidation rate explained in the former section. As shown in Supplementary Fig. 3, the oxidation of aromatic hydrocarbons is completely initiated by OH and Cl radicals.

To quantitatively connect the total reacted aromatic hydrocarbon to Δ[aromatic-OOMs], we must take their respective OOM yields (denoted as Y_{OH} and Y_{Cl}) into account. However, there have been few laboratory studies that report the OOM yield for OH-initiated oxidation of aromatics[76,77], which appears to be substantially lower than that estimated based on ambient observations[30]. And, to the best of our knowledge, there is no study that reports the OOM yield of Cl-initiated oxidation of aromatics. Therefore, it is not feasible to predict the exact value of Δ[aromatic-OOMs] from the total reacted aromatics.

For this reason, we use the correlation coefficient (r) as an indicator to investigate the contribution of OH-initiated and Cl-initiated oxidations with varying relative OOM yields (Y_{Cl}:Y_{OH}). For instance, if Cl-initiated oxidation does not lead to OOM production, that is, Y_{Cl}:Y_{OH} = 0, the inclusion of the reacted aromatics initiated by Cl should clearly reduce the correlation coefficient; vice versa, if Cl-initiated oxidation leads to OOM production, the inclusion of Cl-initiated aromatic oxidation can increase the correlation coefficient. We show Δ[aromatic-OOMs] as a dependent of total reacted aromatics in Extended Data Fig. 8a, in which Y_{Cl}:Y_{OH} is assumed to be 0, 1, 3 and 10 in the respective panels. Here, the test with Y_{Cl}:Y_{OH} = 0 also indicates the case that OOM formation via Cl-initiated oxidation of aromatics is ignored. It can be clearly observed that the correlation becomes stronger when Cl-initiated oxidation of aromatics is considered, supporting our conclusion that Cl contributes a large fraction to the total oxidation of aromatics (Fig. 3d). In addition, we show the variation of the correlation coefficient at different Y_{Cl}:Y_{OH} values in Extended Data Fig. 8b. It seems that the high Y_{Cl}:Y_{OH} (for example, larger than 2) better explains the observation. This is consistent with the reported Y_{Cl}:Y_{OH} for the oxidation of alpha-pinene. Ref. 78 reported an OOM yield of 1.8% for Cl-initiated alpha-pinene oxidation[78], while refs. 79,80 reported an OOM yield of 0.44% and 1.2% for OH-initiated alpha-pinene oxidation, respectively[79,80].

Data availability

The observation data that support the main findings of this study are available at Zenodo (https://doi.org/10.5281/zenodo.8195559). Data on concentrations of air pollutants for Madrid, Helsinki, Los Angeles and San Francisco can be found at https://datos.madrid.es/portal/site/egob, https://smear.avaa.csc.fi/, https://app.cpcbccr.com/ccr/#/caaqm-dashboard-all/caaqm-landing and https://www.arb.ca.gov/aqmis2/aqdselect.php?tab=specialrpt, respectively. Source data are provided with this paper.

Code availability

Data processing techniques are available on request from Chao Yan (chaoyan@nju.edu.cn).

References

41. Liu, Y. et al. Continuous and comprehensive atmospheric observations in Beijing: a station to understand the complex urban atmospheric environment. *Big Earth Data* **4**, 295–321 (2020).
42. Zhou, Y. et al. Variation of size-segregated particle number concentrations in wintertime Beijing. *Atmos. Chem. Phys.* **20**, 1201–1216 (2020).
43. Yan, C. et al. The synergistic role of sulfuric acid, bases, and oxidized organics governing new-particle formation in Beijing. *Geophys. Res. Lett.* **48**, e2020GL091944 (2021).
44. Kulmala, M. et al. Is reducing new particle formation a plausible solution to mitigate particulate air pollution in Beijing and other Chinese megacities? *Faraday Disc.* **226**, 334–347 (2021).
45. Jiang, J., Chen, M., Kuang, C., Attoui, M. & McMurry, P. H. Electrical mobility spectrometer using a diethylene glycol condensation particle counter for measurement of aerosol size distributions down to 1 nm. *Aerosol Sci. Technol.* **45**, 510–521 (2011).
46. Liu, J., Jiang, J., Zhang, Q., Deng, J. & Hao, J. A spectrometer for measuring particle size distributions in the range of 3 nm to 10 μm. *Front. Environ. Sci. Eng.* **10**, 63–72 (2016).
47. Kangasluoma, J. et al. Operation of the airmodus A11 nano condensation nucleus counter at various inlet pressures and various operation temperatures, and design of a new inlet system. *Atmos. Meas. Tech.* **9**, 2977–2988 (2016).
48. Fu, Y., Xue, M., Cai, R., Kangasluoma, J. & Jiang, J. Theoretical and experimental analysis of the core sampling method: reducing diffusional losses in aerosol sampling line. *Aerosol Sci. Technol.* **53**, 793–801 (2019).
49. Cai, R. et al. Aerosol surface area concentration: a governing factor in new particle formation in Beijing. *Atmos. Chem. Phys.* **17**, 12327–12340 (2017).

50. Lee, B. H. et al. An iodide-adduct high-resolution time-of-flight chemical-ionization mass spectrometer: application to atmospheric inorganic and organic compounds. *Environ. Sci. Technol.* **48**, 6309–6317 (2014).
51. Lopez-Hilfiker, F. D. et al. A novel method for online analysis of gas and particle composition: description and evaluation of a Filter Inlet for Gases and AEROsols (FIGAERO). *Atmos. Meas. Tech.* **7**, 983–1001 (2014).
52. Tham, Y. J. et al. Presence of high nitryl chloride in Asian coastal environment and its impact on atmospheric photochemistry. *Chin. Sci. Bull.* **59**, 356–359 (2014).
53. Wang, T. et al. Observations of nitryl chloride and modeling its source and effect on ozone in the planetary boundary layer of southern China. *J. Geophys. Res. Atmos.* **121**, 2476–2489 (2016).
54. Tham, Y. J. et al. Direct field evidence of autocatalytic iodine release from atmospheric aerosol. *Proc. Natl Acad. Sci. USA* **118**, e2009951118 (2021).
55. Jokinen, T. et al. Atmospheric sulphuric acid and neutral cluster measurements using CI-APi-TOF. *Atmos. Chem. Phys.* **12**, 4117–4125 (2012).
56. Kurten, A., Rondo, L., Ehrhart, S. & Curtius, J. Calibration of a chemical ionization mass spectrometer for the measurement of gaseous sulfuric acid. *J. Phys. Chem. A* **116**, 6375–6386 (2012).
57. Atkinson, R. et al. Evaluated kinetic and photochemical data for atmospheric chemistry: Volume I - gas phase reactions of O_x, HO_x, NO_x and SO_x species. *Atmos. Chem. Phys.* **4**, 1461–1738 (2004).
58. Kulmala, M. et al. Measurement of the nucleation of atmospheric aerosol particles. *Nat. Protoc.* **7**, 1651–1667 (2012).
59. Tan, Z. et al. Wintertime photochemistry in Beijing: observations of RO_x radical concentrations in the North China Plain during the BEST-ONE campaign. *Atmos. Chem. Phys.* **18**, 12391–12411 (2018).
60. Heinritzi, M. et al. Characterization of the mass-dependent transmission efficiency of a CIMS. *Atmos. Meas. Tech.* **9**, 1449–1460 (2016).
61. Hyttinen, N. et al. Modeling the charging of highly oxidized cyclohexene ozonolysis products using nitrate-based chemical ionization. *J. Phys. Chem. A* **119**, 6339–6345 (2015).
62. Fröhlich, R. et al. The ToF-ACSM: a portable aerosol chemical speciation monitor with TOFMS detection. *Atmos. Meas. Tech.* **6**, 3225–3241 (2013).
63. Pieber, S. M. et al. Gas-phase composition and secondary organic aerosol formation from standard and particle filter-retrofitted gasoline direct injection vehicles investigated in a batch and flow reactor. *Atmos. Chem. Phys.* **18**, 9929–9954 (2018).
64. Middlebrook, A. M., Bahreini, R., Jimenez, J. L. & Canagaratna, M. R. Evaluation of composition-dependent collection efficiencies for the aerodyne aerosol mass spectrometer using field data. *Aerosol Sci. Technol.* **46**, 258–271 (2012).
65. Viggiano, A., Davidson, J., Fehsenfeld, F. & Ferguson, E. Rate constants for the collisional dissociation of N_2O_5 by N_2. *J. Chem. Phys.* **74**, 6113–6125 (1981).
66. Hahn, J., Luther, K. & Troe, J. Experimental and theoretical study of the temperature and pressure dependences of the recombination reactions $O+NO_2\,(+M)\rightarrow NO_3\,(+M)$ and $NO_2+NO_3\,(+M)\rightarrow N_2O_5\,(+M)$. *Phys. Chem. Chem. Phys.* **2**, 5098–5104 (2000).
67. Brown, S. S., Stark, H. & Ravishankara, A. R. Applicability of the steady state approximation to the interpretation of atmospheric observations of NO_3 and N_2O_5. *J. Geophys. Res.* **108**, 4539 (2003).
68. Brown, S. S. et al. Nighttime chemistry at a high altitude site above Hong Kong. *J. Geophys. Res. Atmos.* **121**, 2457–2475 (2016).
69. Yan, C. et al. Fast heterogeneous loss of N_2O_5 leads to significant nighttime NO_x removal and nitrate aerosol formation at a coastal background environment of southern China. *Sci. Total Environ.* **677**, 637–647 (2019).
70. He, P. et al. Atmospheric $\Delta^{17}O(NO_3^-)$ reveals nocturnal chemistry dominates nitrate production in Beijing haze. *Atmos. Chem. Phys.* **18**, 14465–14476 (2018).
71. Fan, M. et al. Important role of NO_3 radical to nitrate formation aloft in urban Beijing: insights from triple oxygen isotopes measured at the tower. *Environ. Sci. Technol.* **56**, 6870–6879 (2022).
72. Wolfe, G. M., Marvin, M. R., Roberts, S. J., Travis, K. R. & Liao, J. The Framework for 0-D Atmospheric Modeling (F0AM) v3.1. *Geosci. Model Dev.* **9**, 3309–3319 (2016).
73. Jeong, D. et al. Integration of airborne and ground observations of nitryl chloride in the Seoul metropolitan area and the implications on regional oxidation capacity during KORUS-AQ 2016. *Atmos. Chem. Phys.* **19**, 12779–12795 (2019).
74. Haskins, J. D. et al. Anthropogenic control over wintertime oxidation of atmospheric pollutants. *Geophys. Res. Lett.* **46**, 14826–14835 (2019).
75. Wang, X. et al. The role of chlorine in global tropospheric chemistry. *Atmos. Chem. Phys.* **19**, 3981–4003 (2019).
76. Garmash, O. et al. Multi-generation OH oxidation as a source for highly oxygenated organic molecules from aromatics. *Atmos. Chem. Phys.* **20**, 515–537 (2020).
77. Molteni, U. et al. Formation of highly oxygenated organic molecules from aromatic compounds. *Atmos. Chem. Phys.* **18**, 1909–1921 (2018).
78. Wang, Y. et al. Formation of highly oxygenated organic molecules from chlorine-atom-initiated oxidation of alpha-pinene. *Atmos. Chem. Phys.* **20**, 5145–5155 (2020).
79. Jokinen, T. et al. Production of extremely low volatile organic compounds from biogenic emissions: measured yields and atmospheric implications. *Proc. Natl Acad. Sci. USA* **112**, 7123–7128 (2015).
80. Kirkby, J. et al. Ion-induced nucleation of pure biogenic particles. *Nature* **533**, 521–526 (2016).

Acknowledgements

This work is supported by the National Natural Science Foundation of China (NSFC) project (92044301, 42220104006, 42075101 and 41975154), the Academy of Finland (1251427, 1139656, 296628, 306853, 316114 and 311932), the Finnish Centre of Excellence (1141135 and 307331), the European Union's Horizon 2020 programme (ERC, project no.742206 'ATM-GTP', no. 850614 'CHAPAs' and no. 895875 'NPF-PANDA'), the trans-national ERA-PLANET project SMURBS (project no. 689443) under the EU Horizon 2020 Framework Programme, the European Regional Development Fund, the Urban Innovative Actions initiative (HOPE; Healthy Outdoor Premises for Everyone, project no. $UIAO_3^-$ 240), MegaSense by Business Finland (grant no. 7517/31/2018) and Academy of Finland Flagship funding (grant no. 337549). The Beijing University of Chemical Technology team is supported by the National Natural Science Foundation of China (42275117) and the Beijing Natural Science Foundation (8232041). Y.J.T. acknowledges the funding support from the National Natural Science Foundation of China (42175118) and the Guangdong Basic and Applied Basic Research Foundation (2022A1515010852). The CSIC team acknowledges the funding support from the European Research Council Executive Agency under the European Union's Horizon 2020 Research and Innovation Programme (project ERC-2016-COG, project no. 726349 CLIMAHAL to A.S.-L.). The Tsinghua University team acknowledges the National Natural Science Foundation of China (22188102) and Samsung $PM_{2.5}$ SRP. N.M.D. acknowledges the US National Science Foundation grant AGS2132089. H.W. acknowledges the funding support from the National Natural Science Foundation of China (42175111). The Indian Institute of Tropical Meteorology is funded by the Ministry of Earth Sciences, Government of India. We acknowledge the German federal

environmental agency for kindly providing us with the O_3, NO_x and $PM_{2.5}$ and PM_{10} data in Frankfurt and Berlin. The data at the Frankfurt sites were measured by Hessisches Landesamt für Naturschutz, Umwelt und Geologie and the data at the Berlin sites were measured by Senatsverwaltung für Umwelt, Mobilität, Verbraucher- und Klimaschutz. We thank them for their great effort. We acknowledge the Madrid Air Quality Monitoring Network, Smart SMEAR Network, India Central Pollution Control Board and California Air Resources Board for the NO_x, O_3, CO and $PM_{2.5}$ open data sources. We thank X. Huang and the modelling group at Nanjing University for their useful discussion regarding the vertical distribution of air pollution.

Author contributions

C.Y., Y.J.T., A.D. and M.K. designed the study. C.Y., Y.J.T, W.N, H.W., Y.G., W.M., J.Z., C.H., Yu.L., C.D., Yi.L., F.Z., X.C., G.Z., D.D.H., Z.W., Y.S., F.B., J.J., D.R.W. and Y. Liu collected and analysed the data. M.X, Q.L., A.S.M., C.A.C. and A.S.-L. conducted the model development and simulations. C.Y., Y.J.T., V.-M.K., N.M.D. and M.K. wrote the manuscript. All authors participated in relevant scientific discussions and commented on the manuscript.

Competing interests

The authors declare no competing interests.

Additional information

Extended data is available for this paper at https://doi.org/10.1038/s41561-023-01285-1.

Supplementary information The online version contains supplementary material available at https://doi.org/10.1038/s41561-023-01285-1.

Correspondence and requests for materials should be addressed to Yee Jun Tham, Aijun Ding or Markku Kulmala.

Peer review information *Nature Geoscience* thanks Matthias Beekmann and the other, anonymous, reviewer(s) for their contribution to the peer review of this work. Primary Handling Editor: Xujia Jiang, in collaboration with the *Nature Geoscience* team.

https://doi.org/10.1038/s41561-023-01285-1

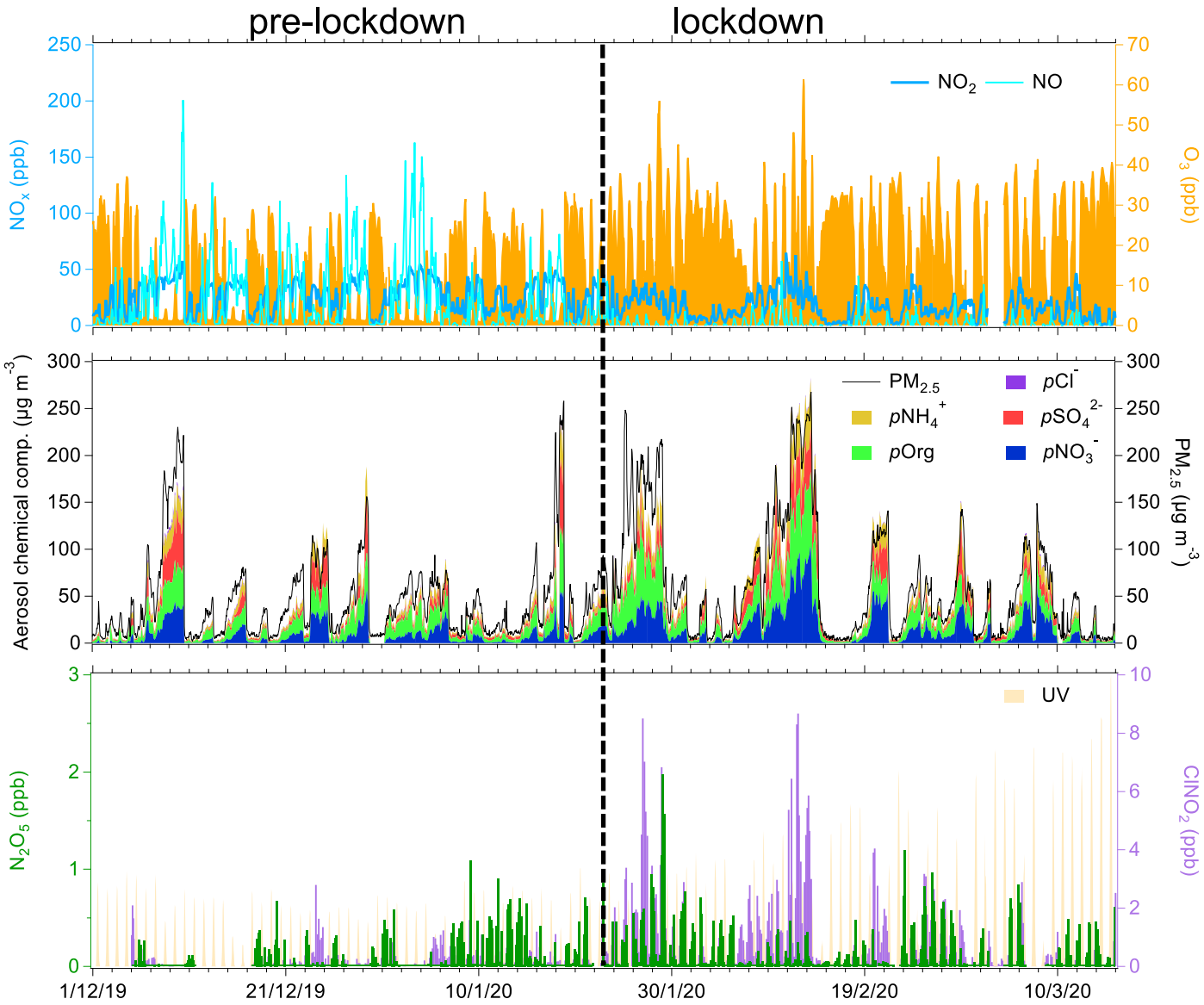

Extended Data Fig. 1 | Time series of reactive nitrogen species, including NO, NO_2, N_2O_5, $ClNO_2$, and $PM_{2.5}$ chemical composition before and after lockdown. The yellow-shaded areas denote daytime. As explained in the text, the dashed vertical line represents the separation of the pre-lockdown and lockdown periods.

https://doi.org/10.1038/s41561-023-01285-1

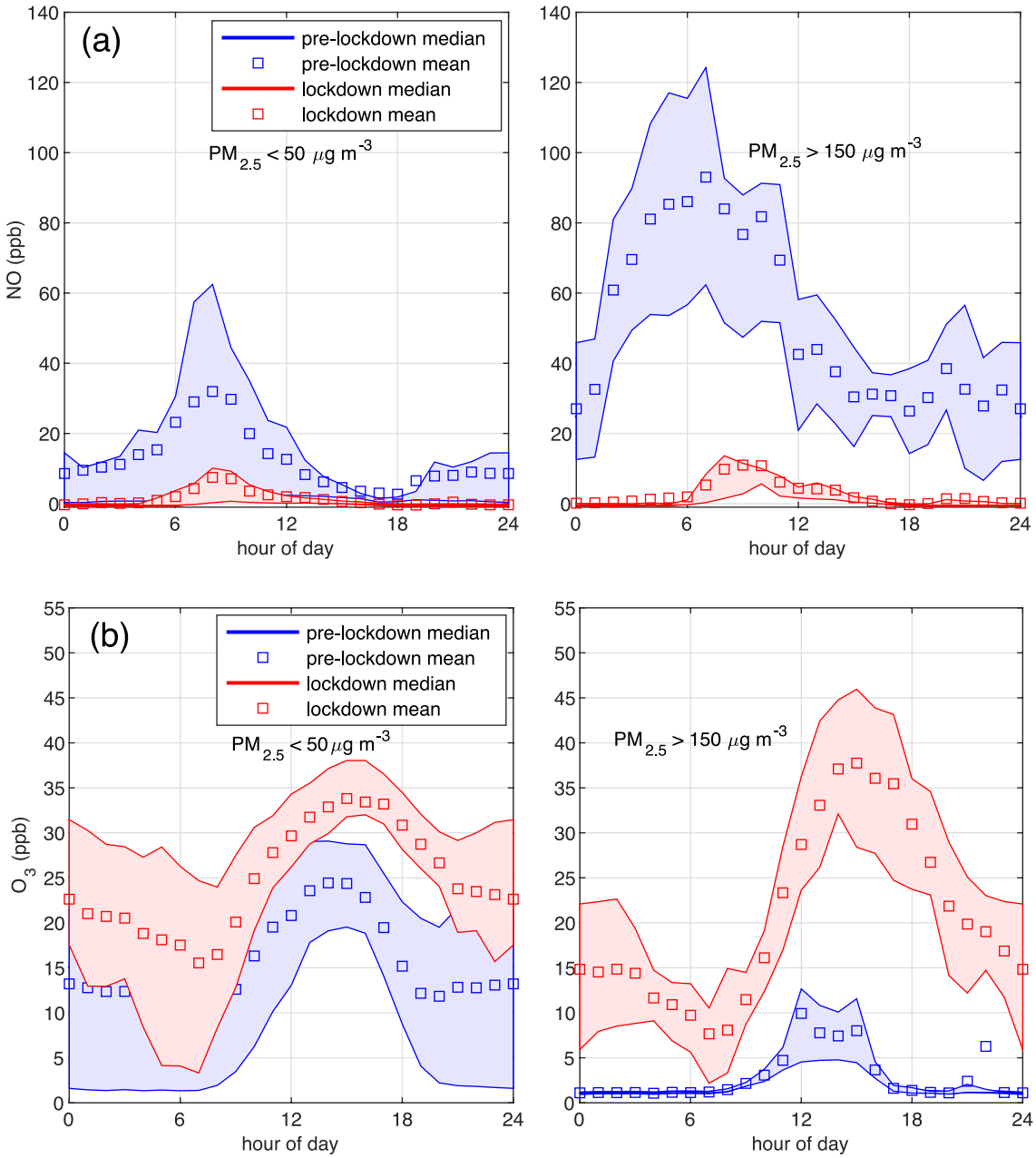

Extended Data Fig. 2 | Diurnal variations of NO (a) and O_3 (b) concentrations in the pre-lockdown and lockdown periods. Data of clean conditions ($PM_{2.5}$ < 50 μg m^{-3}) and during polluted conditions ($PM_{2.5}$ > 150 μg m^{-3}) on the left and right panels, respectively. The solid lines denote the median values, shaded areas represent the range of 25 %–75 % variations, and empty squares indicate the mean values.

https://doi.org/10.1038/s41561-023-01285-1

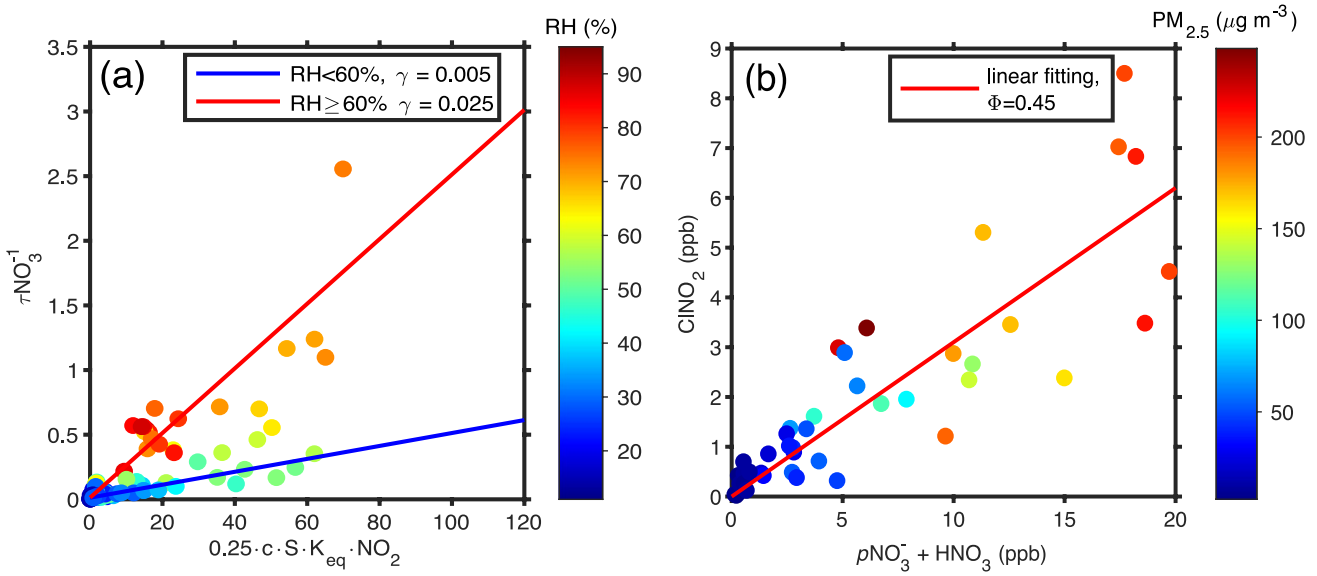

Extended Data Fig. 3 | Derivation of N_2O_5 uptake coefficients (γ) using the linear-regression method (see Methods) (a) and determination of $ClNO_2$ yield (b). In Panel (a), the $(\tau NO_3)^{-1}$ is the inverse of NO_3 lifetime, c denotes the molecular speed of N_2O_5 that is 240 m s^{-1}, S denotes the concentration of particle surface area, and K_{eq} denotes the equilibrium rate constant between NO_3 and N_2O_5. In this plot, the slope and intersect of the linear regression indicate uptake coefficient and k_{NO3}, respectively. Data are color-coded by RH, which has a major influence on the slope. In Panel (b), the mass concentration of nitrate is converted to a mixing ratio. The slope that equals $\phi / (2-\phi)$ is fitted as 0.29, and hence ϕ is calculated as 0.45. Since nitrate formation through N_2O_5 heterogeneous reaction is very limited in the pre-lockdown period, we only use data in the lockdown period to determine the uptake coefficient of N_2O_5 and the yield of $ClNO_2$.

https://doi.org/10.1038/s41561-023-01285-1

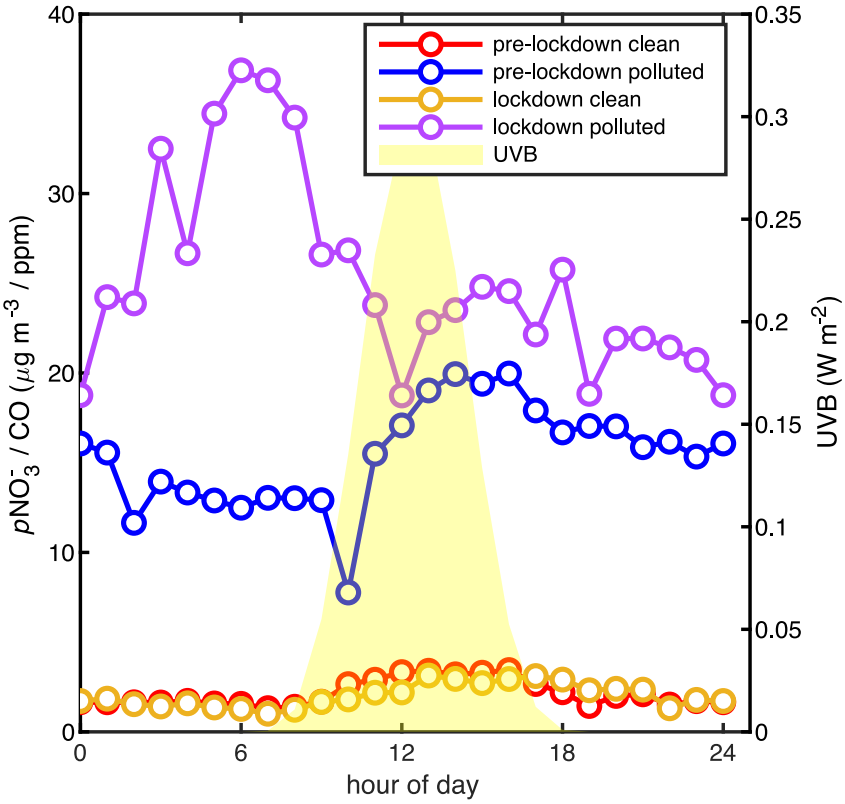

Extended Data Fig. 4 | Diurnal patterns of pNO_3^- in different pollution scenarios. Clean and polluted conditions are defined as $PM_{2.5} < 50\ \mu g\ m^{-3}$ and $PM_{2.5} > 150\ \mu g\ m^{-3}$, respectively. The concentration of pNO_3^- is normalized to CO mixing ratio to eliminate the possible influence of air mass transport and fresh emission.

https://doi.org/10.1038/s41561-023-01285-1

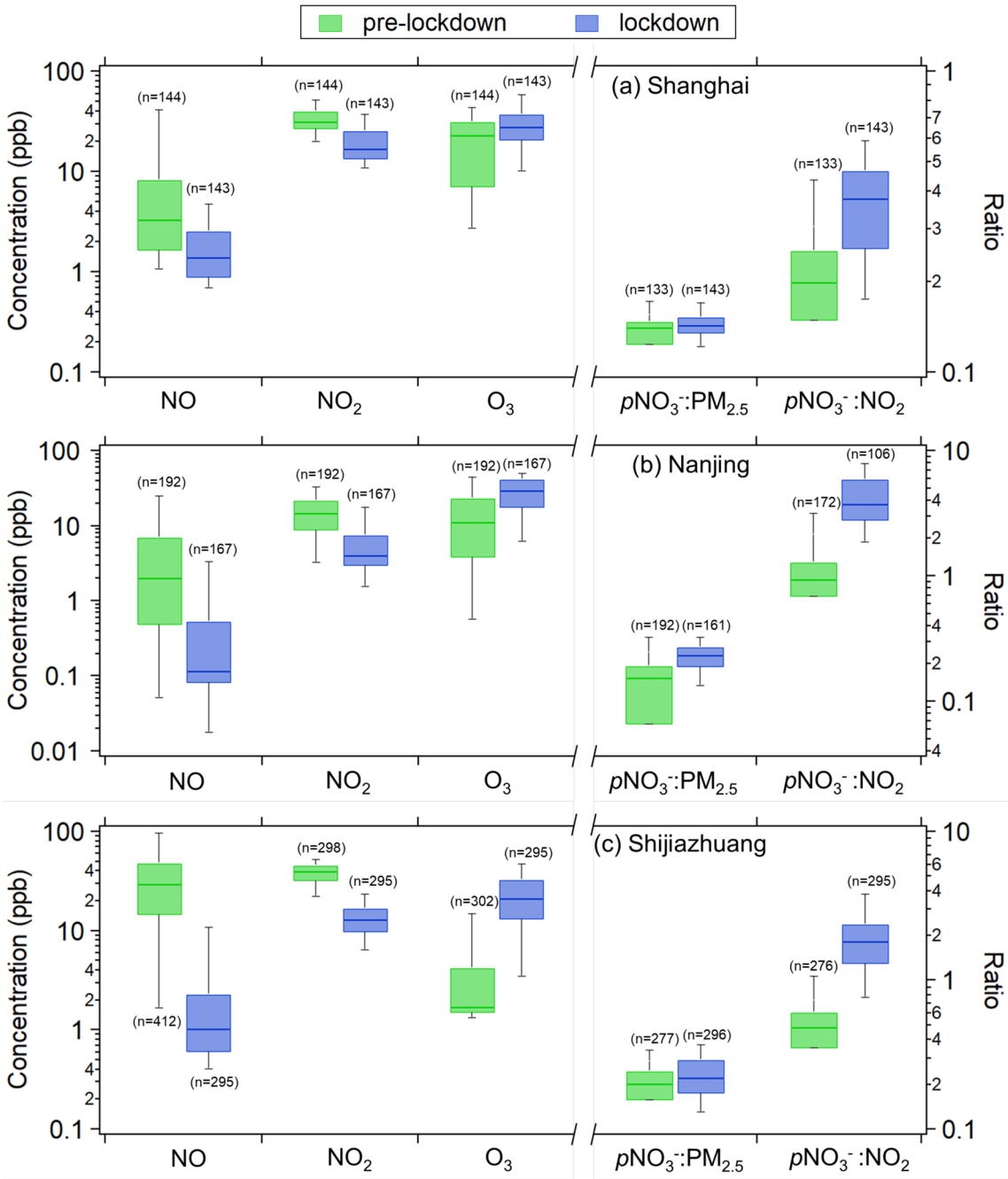

Extended Data Fig. 5 | Comparisons of NO, NO2, O3 concentrations, pNO3-/PM2.5, and pNO3-/NO2 between the pre-lockdown and lockdown periods from different cities in China. Panels **a**, **b**, and **c** show the results from Shanghai, Nanjing, Shijiazhuang, respectively. The centre, bounds of box and whiskers represent the median, 25 (75) percentiles, and 5 (95) percentiles of the data, respectively. Note that only data from polluted nights were used for this analysis. As the averaged PM2.5 level differs in NCP and YRD, the polluted condition is defined as PM2.5 > 150 μg m-3 for Shijiazhuang and PM2.5 > 75 μg m-3 for Nanjing and Shanghai.

https://doi.org/10.1038/s41561-023-01285-1

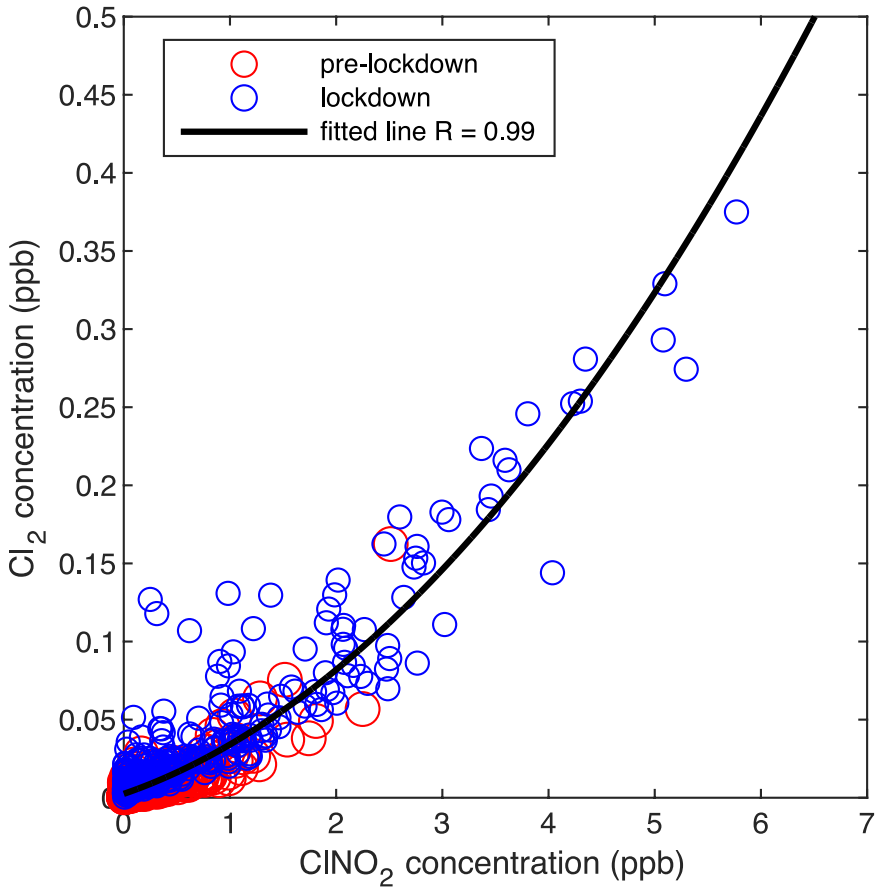

Extended Data Fig. 6 | The strong correlation (R = 0.99) between $ClNO_2$ and Cl_2. Red and blue empty circles denote data collected during the pre-lockdown and lockdown periods, respectively.

https://doi.org/10.1038/s41561-023-01285-1

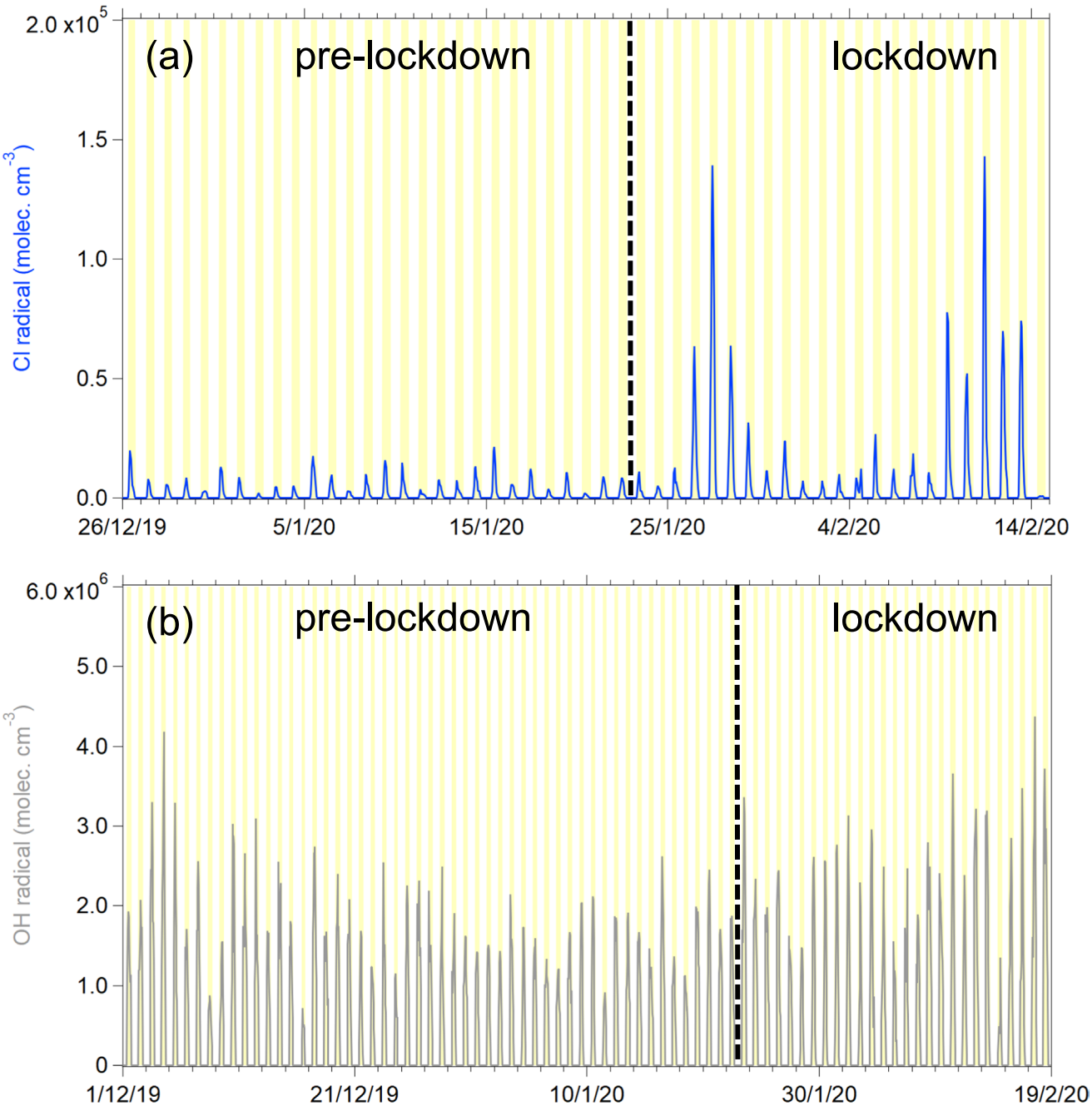

Extended Data Fig. 7 | Time series of estimated Cl and OH concentrations. Panels **a** and **b** show the time series of simulated Cl radical and OH radical, respectively. The details of the estimation are provided in Methods. The yellow-shaded area represents the daytime.

https://doi.org/10.1038/s41561-023-01285-1

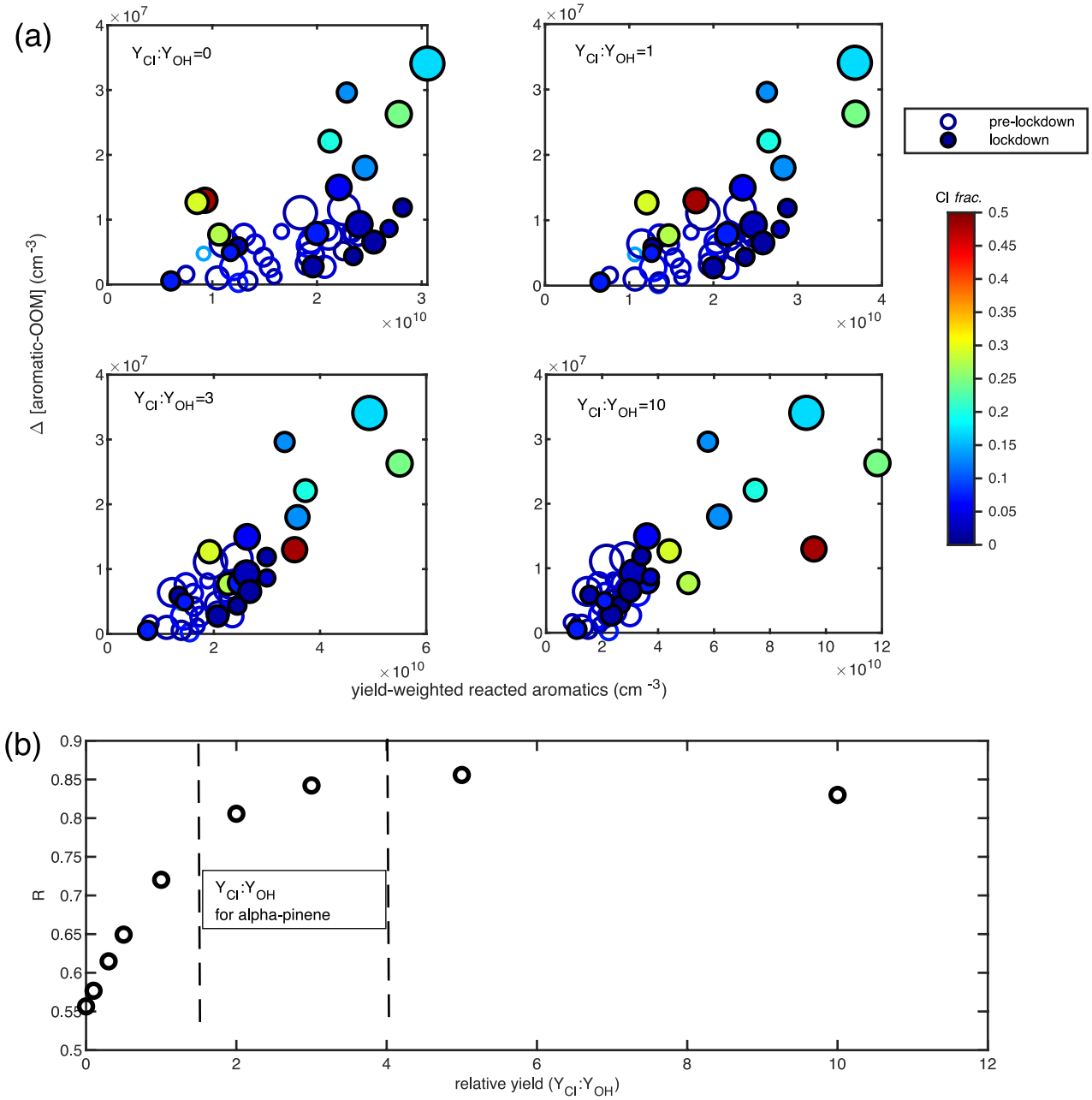

Extended Data Fig. 8 | The increase of aromatic-OOM concentration (Δ[aromatic-OOM]) as a dependent of reacted monocyclic aromatics weighted by OOM yield. (**a**), and the correlation coefficient between Δ[aromatic-OOM] and the yield-weighted reacted aromatics. In panel (a), Δ[aromatic-OOM]$_i$ is calculated as the difference between the daily maximum and minimum aromatic-OOM concentration, as illustrated in Supplementary Fig. 1 in Supporting Information. The calculation of yield-weighted reacted aromatics is demonstrated in detail in Methods. In panel (**b**), the two dashed lines denote the range of relative OOM yield (Y_{Cl}:Y_{OH}) obtained for alpha-pinene oxidation in previous studies.

https://doi.org/10.1038/s41561-023-01285-1

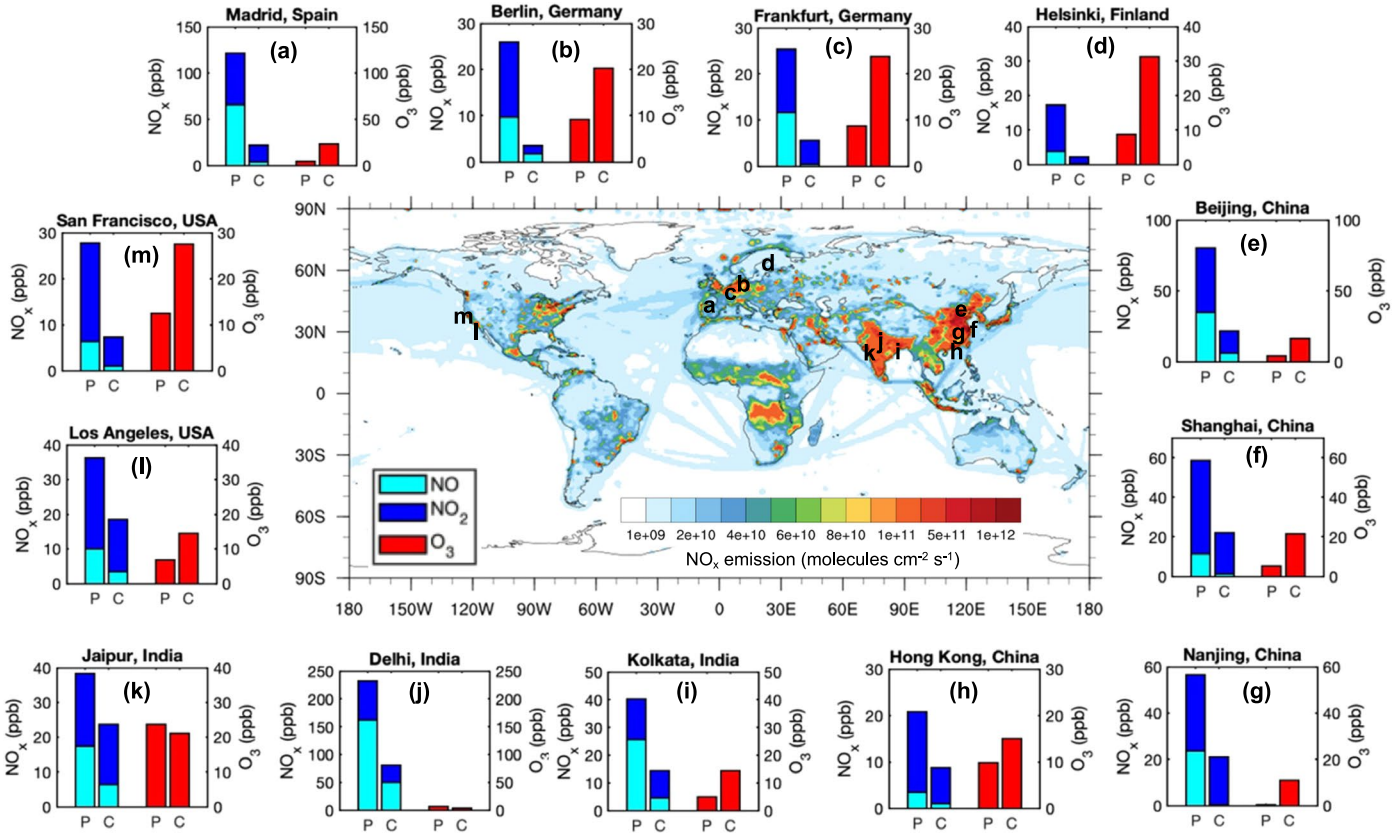

Extended Data Fig. 9 | Observations of nighttime NO_x (NO and NO_2) and O_3 levels in major cities around the globe. The world map illustrates the global NO_x emission in 2020. The corresponding location of the city is shown by an alphabet (**a**–**m**) on the map. The reported NO (cyan bar), NO_2 (blue bar), and O_3 (red bar) data are the average values between 10 p.m. and 4 a.m. (local time) during the winter. Relatively polluted (denoted by 'P') and clean (denoted by 'C') conditions are separated based on $PM_{2.5}$ levels, or CO concentrations if $PM_{2.5}$ concentration is not available. In cities with high pollution levels (that is, cities in China and India), 'P' and 'C' conditions are separated based on $PM_{2.5} < 50\ \mu g\ m^{-3}$ and $PM_{2.5} > 150\ \mu g\ m^{-3}$, respectively. In European and US cities, where $PM_{2.5}$ barely exceeded $150\ \mu g\ m^{-3}$, 25 and 75 quantiles of $PM_{2.5}$ (or CO, when the $PM_{2.5}$ is not available) are used to define the relatively polluted and clean conditions. Details of the measurement sites, durations, and data sources are provided in Table S2 in the Supplementary Information.

nature geoscience

Article

https://doi.org/10.1038/s41561-023-01285-1

Increasing contribution of nighttime nitrogen chemistry to wintertime haze formation in Beijing observed during COVID-19 lockdowns

In the format provided by the authors and unedited

Table of Contents:

Evaluation of the vertical distribution of pNO_3^- production using a 3-D model

One major aspect of the "inherent disconnect" concerns the representativeness of ground-based measurements to the entire boundary layer, which is a significant limitation of this research topic. Conducting measurements in the residual layer well above 300 m with heavy, sophisticated instruments such as the iodide CIMS is technically challenging. As far as we know, there are no such measurements in China. As suggested by the reviewer, we deployed a 3-D model (WRF-Chem) to explore this issue. This model has been previously used to evaluate the impact of COVID-19 lockdown on air pollution in East China[14], where all details of the modeling setup are illustrated. The vertical profiles of NO, NO_2, and O_3 concentrations, were scaled based on the ratio between modeled (28 m height) and measured concentrations before further analysis. The total heterogeneous loss rate of N_2O_5 is calculated as the difference between the total production rate of NO_3 and N_2O_5 and the loss of NO_3 to NO (see Eq. R1), with an assumption that the loss rate of N_2O_5 is γ-insensitive under high particle loadings[16]. Then the production rate of pNO_3^- is calculated based on the yield of N_2O_5 as derived in our study (Eq. R2).

$L(N_2O_5) = k1[NO_2][O_3] - k2[NO][NO_3]$ (Eq. R1)

$P(pNO_3^-) = (2 - \Phi)\, L(N_2O_5)$ (Eq. R2)

Here, $k_1 = 1.4\times10^{-13}\exp(-2470/T)$, $k_2 = 1.8\times10^{-11}\exp(110/T)$, and $\phi = 0.45$.

Figure R2-5 displays the modeled vertical profiles of NO, NO_2, O_3 concentrations, and the calculated production rate of pNO_3^- during severe haze episodes in both pre-lockdown and lockdown periods. The simulations indicate that while significant amounts of pNO_3^- were formed in the residual layer (above ~500 m) in the pre-lockdown period, the formation was much more limited in the lockdown period due to low NO_2 concentration. This suggests that the contribution of the N_2O_5 pathway to pNO_3^- may have been underestimated

during the pre-lockdown period but overestimated during the lockdown period. Nonetheless, the column-mean production rate of pNO_3^- during the lockdown period was estimated to be approximately three times larger than that in the pre-lockdown period, supporting our conclusion on enhanced nocturnal nitrogen chemistry. It is important to note that the accuracy of the 3-D modeling is not strictly validated with *in situ* observations, and thus all values shown in the figure should only be regarded as qualitative.

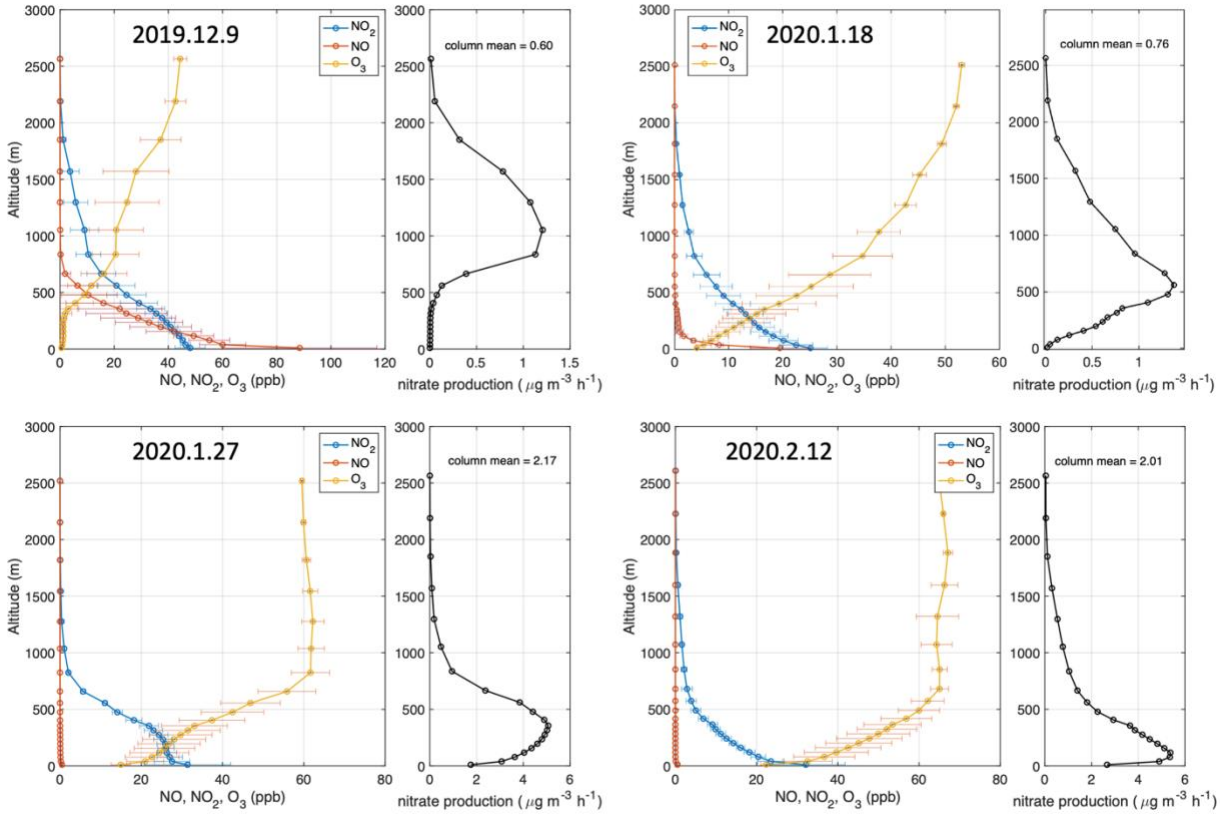

Figure S1. Simulated vertical profiles of NO, NO_2, and O_3 concentrations, as well as the calculated pNO_3^- production rate. The upper two panels are severe haze episodes in the pre-lockdown period, and the lower two panels are severe haze episodes in the lockdown periods. The error bar denotes the 1σ standard deviation of modeled concentration during the whole night. The relative error of the calculated pNO_3^- production rate is estimated to be less than $\pm$ 50 %.

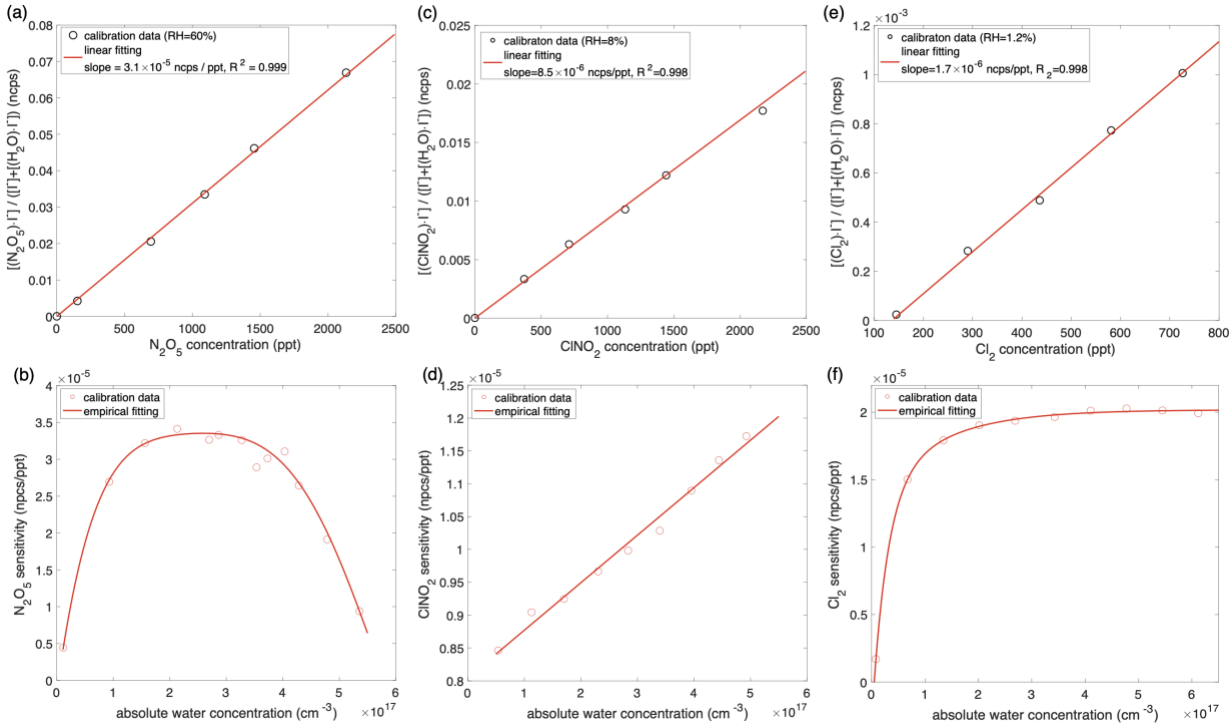

Fig. S2. Calibrations of N_2O_5, $ClNO_2$, and Cl_2, including multipoint calibrations at a constant RH (and constant water vapor concentration) (a, c, e) and calibrations of the sensitivity at varying concentrations of water vapors (b,d,f). Strong linearity can be seen in all calibration sets ($R^2 \geq 0.998$) for the multipoint calibration, and linear regression is used to derive the sensitivities. The dependence of sensitivities on water vapor concentration show different patterns, for which empirical fitting equations are used (red solid lines in Panels b, d, and f).

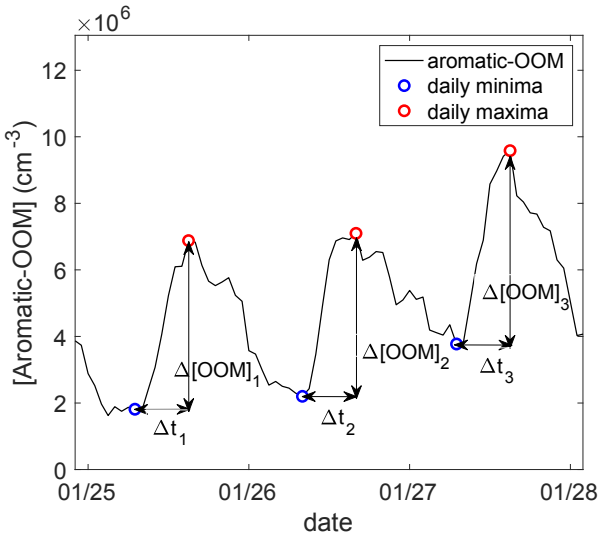

Fig. S3. Determination of Δ[aromatic-OOM] and its corresponding time window. Δ [aromatic-OOM]$_i$ is calculated on a daily basis as the difference between the minimum (blue circles) and maximum (red circles) of aromatic-OOM concentration; the corresponding time duration is defined as Δt_i.

Table S1. VOC and its reaction rate coefficient used for the calculation of VOC oxidation rate.

Formula	VOC	Adopted reaction rate coefficient, k (cm^3 $molecule^{-1}$ s^{-1})			
		with Cl	with OH	with NO_3	with O_3
C_6H_6	Benzene	1.30×10^{-15}	1.20×10^{-12}	1.10×10^{-17}	1.00×10^{-21}
C_7H_8	Toluene	6.20×10^{-11}	5.60×10^{-12}	2.01×10^{-17}	1.00×10^{-21}
C_8H_{10}	Ethylbenzene	1.15×10^{-10}	7.51×10^{-12}	5.71×10^{-16}	8.48×10^{-22}
C_9H_{12}	1,3,5-trimethylbenzene	1.94×10^{-10}	6.26×10^{-11}	8.00×10^{-16}	2.91×10^{-21}
$C_{10}H_{14}$	*p*-cymene	1.72×10^{-10}	4.85×10^{-12}	1.00×10^{-15}	5.00×10^{-20}
$C_{10}H_8$	Naphthalene	3.82×10^{-12}	3.69×10^{-11}	*n/a*	2.01×10^{-19}
C_4H_{10}	*n*-Butane	2.05×10^{-10}	2.30×10^{-12}	3.43×10^{-17}	1.00×10^{-23}
C_6H_{12}	Cyclohexane	2.01×10^{-10}	5.28×10^{-12}	1.35×10^{-16}	7.82×10^{-18}
C_4H_8	1-Butene	2.56×10^{-10}	3.48×10^{-11}	1.06×10^{-14}	6.72×10^{-18}
C_6H_{10}	Cyclohexene	3.49×10^{-10}	6.09×10^{-11}	6.58×10^{-13}	5.52×10^{-17}
C_5H_8	Isoprene	4.30×10^{-10}	1.00×10^{-10}	5.88×10^{-13}	7.20×10^{-18}

Note that *n/a* means the *k* for this reaction is not available.

Table S2. Details of the NO_x, O_3, $PM_{2.5}$, and CO measurements. The hourly data during wintertime were obtained from our measurements and open data sources.

	Site	Location	Site types	Data period
Europe	(a) Madrid, Spain	Escuelas Aguirre*	Urban	Feb, 2019
	(b) Berlin, Germany	Neukölln	Urban background	Dec, 2016, Jan, Feb, and Dec, 2017, Jan and Feb, 2018
	(c) Frankfurt, Germany	Schwanheim	Urban background	Dec, 2016, Jan, Feb, and Dec, 2017, Jan and Feb, 2018
	(d) Helsinki, Finland	Kumpula campus of University of Helsinki **	Urban	Jan, Feb, and Dec, 2019-2021, Jan and Feb, 2022
Asia	(e) Beijing, China	West campus of Beijing University of Chemical Technology	Urban	Jan, Feb, and Dec, 2019 Jan 1 – 22, 2020
	(f) Shanghai, China	Shanghai Academy of Environmental Sciences	Urban	Dec, 2019-2020, Jan and Dec, 2021, Jan, 2022
	(g) Nanjing, China	SORPES monitoring station	Suburban	Dec, 2020, Jan, 2021
	(h) Hong Kong, China	Tung Chung monitoring station	Suburban	Dec, 2021, Jan and Feb, 2022
	(i) Kolkata, India	Bidhannagar, Kolkata - WBPCB***	Urban	Nov-Dec, 2019
	(j) Delhi, India	CRRI Mathura Road, Delhi – IMD***	Urban	Nov-Dec, 2019
	(k) Jaipur, India	Adarsh Nagar, Jaipur - RSPCB***	Urban	Nov-Dec, 2019
North America	(l) Los Angeles, USA****	Pasadena-S Wilson Avenue****	Suburban	Nov-Dec, 2019
	(m) San Francisco, USA****	San Francisco-Arkansas Street****	Urban	Nov-Dec, 2019

Note: Websites of open data sources:
* https://datos.madrid.es/portal/site/egob;
** https://smear.avaa.csc.fi/ ;
*** https://app.cpcbccr.com/ccr/#/caaqm-dashboard-all/caaqm-landing;
**** https://www.arb.ca.gov/aqmis2/aqdselect.php?tab=specialrpt